

2006

## Designing and testing a nulling radially symmetric microellipsometer

Alain Ngoy Tschimwang  
*University of Dayton*

Follow this and additional works at: [https://ecommons.udayton.edu/graduate\\_theses](https://ecommons.udayton.edu/graduate_theses)

---

### Recommended Citation

Tschimwang, Alain Ngoy, "Designing and testing a nulling radially symmetric microellipsometer" (2006).  
*Graduate Theses and Dissertations*. 6042.  
[https://ecommons.udayton.edu/graduate\\_theses/6042](https://ecommons.udayton.edu/graduate_theses/6042)

This Thesis is brought to you for free and open access by the Theses and Dissertations at eCommons. It has been accepted for inclusion in Graduate Theses and Dissertations by an authorized administrator of eCommons. For more information, please contact [mschlangen1@udayton.edu](mailto:mschlangen1@udayton.edu), [ecommons@udayton.edu](mailto:ecommons@udayton.edu).

**DESIGNING AND TESTING A NULLING RADially  
SYMMETRIC MICROELLIPSOMETER**

Thesis

Submitted to

The School of Engineering of the

UNIVERSITY OF DAYTON

in Partial Fulfillment of the Requirement for

The Degree

Master of Science in Electro-Optics

by

Alain Ngoy Tschimwang

UNIVERSITY OF DAYTON

Dayton, Ohio

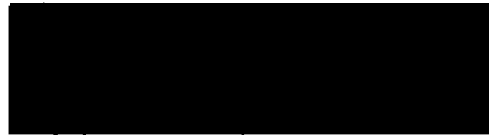
December, 2006

## DESIGNING AND TESTING A NULLING RADIALY SYMMETRIC MICROELLIPSOMETER

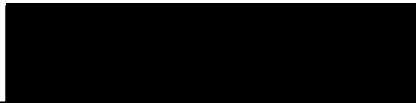
APPROVED BY:



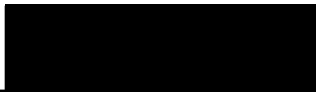
Qiwen Zhan, Ph.D.  
Advisory Committee Chairman  
Assistant Professor, Electro-Optics  
and Electrical/Computer Engineering  
Departments



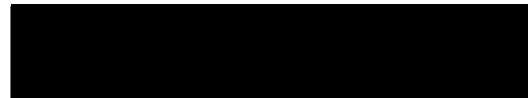
Joseph Haus, Ph.D.  
Committee Member  
Professor and Chair  
Electro-Optics Department



John Loomis, Ph.D.  
Committee Member  
Professor, Electro-Optics and  
Electrical/Computer Engineering  
Departments



Donald L. Moon, Ph.D.  
Associate Dean  
Graduate Engineering Programs &  
Research  
School of Engineering



Joseph E. Saliba, Ph.D., P.E.  
Dean, School of Engineering

## **ABSTRACT**

### **DESIGNING AND TESTING A RADIALY SYMMETRIC MICROELLIPSOMETER**

Tschimwang, Alain, Ngoy  
University of Dayton

Advisor: Dr. Qiwen Zhan

Ellipsometry is a powerful optical metrology technique used to measure thin films properties such as thickness and refractive index simultaneously and in a non-destructive way. Most ellipsometers available in the market suffer from a limitation in the spatial resolution and this problem makes this technique inadequate for characterizing microstructured thin films and surfaces. Another difficulty in microellipsometry is a low signal-to-noise (SNR) ratio due to the detector's pixel size required for good ellipsometric performance. In this thesis a nulling microellipsometer design using a radial symmetry concept has been implemented and tested. The radial symmetry is achieved by passing a circularly polarized beam through an electro-optical variable retarder and a radial analyzer. A high numerical aperture objective is used to achieve high angle illumination of the sample and tight focusing of the beam on the sample. Due to their symmetry, the rays within the entire annular ring in the back focal plane, instead of just one small portion of the ring as it is the case with a back focal plan microellipsometer,

act like individual signal channels that contribute equally and collaboratively to the total signal. The nulling scheme of this device is performed by an electro-optical circular retarder that allows a fast signal modulation, i.e. fast data collection. The microellipsometer is automated using the Labview's GPIB interface. The instrument was tested using a sample on which some patterns were lithographically etched. The results of the tests are presented and analyzed and further improvements have been suggested for future work.

## **ACKNOWLEDGEMENTS**

First, praise be to you Lord of host for your infinite wisdom and goodness to me. May this intellectual work lift up your glory.

I would like to thank my advisor, Dr. Qiwen Zhan, for his guidance and leading advice, especially for having spent countless hours with me in the microellipsometry laboratory. I would like to thank Dr. Joseph Haus for his encouragement and moral support to me from the beginning to the end of this work.

To my dear mother, father, sisters, and brothers, I say thank you for your prayers, love and support. Though far away from me, you have always been in my heart. I dedicate this work to my late sister Norris Kabange Kabey - A - Tshimwang.

## TABLE OF CONTENTS

ABSTRACT .....	iii
ACKNOWLEDGEMENTS .....	v
LIST OF FIGURES .....	viii
INTRODUCTION .....	1
Basics of Reflection and Polarization .....	1
Multiple Reflections on a Multi-layered Medium .....	4
Ellipsometric Definitions .....	5
CHAPTER:	
I. THE BASICS OF ELLIPSOMETRY .....	7
Brief Historical Background .....	7
Common Optical Elements Used in Ellipsometry .....	8
Common Ellipsometer Arrangements .....	10
<i>Nulling Ellipsometer</i> .....	11
<i>Rotating elements Ellipsometer</i> .....	13
<i>The PSRA Ellipsometer</i> .....	16
II. NEW DEVELOPMENTS AND ISSUES IN ELLIPSOMETRY .....	19
III. DESIGN OF A RADIALY SYMMETRIC -	
MICROELLIPSOMETER .....	22

Fundamentals of the Design .....	22
Signal Derivation and Nulling Scheme Implementation .....	27
IV. INSTRUMENTATION AND TESTING .....	30
Instrumentation .....	30
Modulator Calibration and System Alignments .....	34
Signal Testing and Processing .....	37
Preliminary Results and Analysis .....	43
Manually Processed Data and Discussions .....	49
Summary .....	55
V. FUTURE WORK .....	56
Signal Strength and Quality .....	56
Using Radially Polarized Light for Sample Illumination .....	57
Calculating the Optical Properties .....	60
Improving the User Interface .....	60
BIBLIOGRAPHY .....	61



## LIST OF FIGURES

Figure 1: .....	1
Polarization reflections at an interface	
Figure 2: .....	2
Reflection at single interface	
Figure 3: .....	3
3(a): S and P reflection coefficients vs. incident angle	
3(b): S and P power reflection coefficients vs. incident angle	
Figure 4: .....	4
Multiple reflections at a multi-layered medium interface	
Figure 5: .....	11
Conceptual Nulling Ellipsometer	
Figure 6: .....	12
A conceptual nulling arrangement with the QWP inserted before the sample.	
Figure 7: .....	13
Intensity vs. polarizer's angle near the null	
Figure 8: .....	14
A rotating null ellipsometer arrangement	

Figure 9: .....	16
Rotating null ellipsometer (figure published in reference [5])	
Figure 10: .....	17
PSRA ellipsometer basic arrangement	
Figure 11: .....	22
(a) A standard ellipsometer	
(b) After a high NA lens insertion	
Figure 12: .....	23
Conceptual diagram of radially symmetric microellipsometer design	
Figure 13: .....	25
Diagram of the EO circular variable retarder	
Figure 14: .....	27
Coordinate systems used for signal derivation	
Figure 15: .....	30
The complete laboratory setup of the microellipsometer	
Figure 16: .....	33
The three loops in charge of instruments control and signal processing	
Figure 17: .....	34
Polarization rotator calibration setup	
Figure 18: .....	35
Polarization rotator calibration curve	
Figure 19: .....	37
Setup used to generate circularly polarized light in the objective's back focal plane	

Figure 20(a): .....	38
Detected signal amplitude when circular polarization is used	
Figure 20(b): .....	38
Detected signal amplitude when quasi-circular polarization is used	
Figure 20(c): .....	39
Detected signal amplitude when linear polarization is used	
Figure 20(d): .....	39
General polarization signal for different values of $\Phi_b$	
Figure 21: .....	40
Modulation a.c voltage (top) and the detected 2 <sup>nd</sup> harmonic signal (bottom) obtained while testing the polarization rotator and the null detection	
Figure 22: .....	41
(a) Total signal	
(b) Null occurrence (2 <sup>nd</sup> harmonic)	
Figure 23: .....	42
Signal shapes (a) Max-min-max case; (b) Min-max-min case	
Figure 24(a): .....	44
Pattern topography	
Figure 24(b): .....	44
Line profile of a trench	
Figure 25: .....	45
First test: minimum amplitude voltage vs. scanned position	
Figure 26 (a): .....	46

Result repeatability test: minimum amplitude voltage vs. scanned position	
Figure 26(b): .....	47
Result repeatability test: minimum amplitude voltage vs. scanned position	
Figure 27: .....	48
(a) Ray picture of reflection on a rough surface. (b) The focal spot seats on an edge	
Figure 28: .....	49
Manually processed data of the minimum voltage vs. scanned position on the sample	
Figure 29: .....	50
Signal amplitude data display. Dark regions are amplitude minima	
Figure 30: .....	52
Repeatability test: minimum amplitude voltage vs. position on the sample	
Figure 31: .....	54
(a) – (b): Signal amplitude data: Amplitude evolution in bias voltage and location on the sample. The dark regions show the evolution of the minima.	
Figure 32: .....	58
(a) – (d): Signals produced by circular and quasi-circular Polarizations.	
Figure 33: .....	59
Radial polarization illumination	

## INTRODUCTION

### A. The Basics of Reflection and Polarization

Ellipsometry is generally defined as a technique of measuring the state of polarization of a polarized wave [1]. Ellipsometry is divided in two major areas: one is transmission ellipsometry, also often known as polarimetry, and the other is reflection ellipsometry. In transmission ellipsometry the change of polarization is measured in the transmitted fields whereas in reflection ellipsometry this change of polarization is measured in the reflected fields. In this work we will definitively assume the latter case whenever the term “ellipsometry” is mentioned. Since this work is entirely based upon reflection ellipsometry, the basic law of reflection is briefly reviewed below.

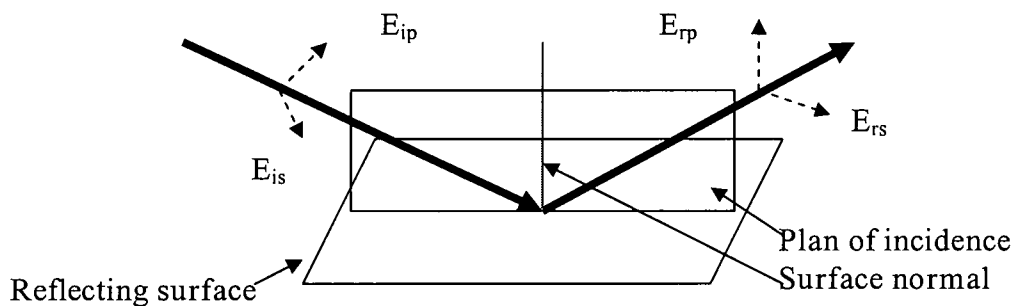


Figure 1. Polarization reflections at an interface

When an electro-magnetic field with s and p polarizations is incident on a sample medium as shown in Figure 1, generally the reflected field polarization components,

s and p, are reflected differently as the incident field picks up a phase and an amplitude upon reflection. Consider that the ambient medium of figure 1 has an index of refraction  $n_1$ . Suppose that the reflecting surface is a surface of a medium whose index of refraction is  $n_2$ . The amplitudes of the reflected polarization components will be equal to those of the incident polarization components weighed by their respective reflection coefficients. These coefficients are known as “Fresnel coefficients” [2]. Considering the simple case where the beam is reflecting from a single interface as shown in figure 2, if  $\Phi_1$  and  $\Phi_2$  are the incidence and refraction angles, respectively, the Fresnel coefficients can be written as

$$r_{12}^p = \frac{n_2 \cos \Phi_1 - n_1 \cos \Phi_2}{n_2 \cos \Phi_1 + n_1 \cos \Phi_2}, \quad r_{12}^s = \frac{n_1 \cos \Phi_1 - n_2 \cos \Phi_2}{n_1 \cos \Phi_1 + n_2 \cos \Phi_2} \quad (1)$$

for the p and s polarization components, respectively. In the case of multiple interface reflection these coefficients are generally complex, i.e, they have a magnitude and a phase, but for a single interface reflection as shown in figure 2 the coefficients are always real. At normal incidence, i.e  $\Phi_1 = \Phi_2 = 0^\circ$ , the coefficients are

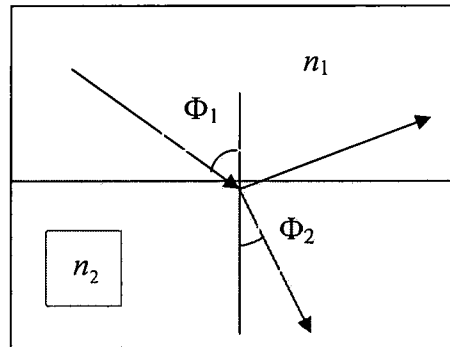


Figure 2. Reflection at a single interface

reduced to their much simpler form as

$$r_{12}^p = \frac{n_2 - 1}{n_2 + 1}, \quad r_{12}^s = \frac{1 - n_2}{1 + n_2}, \quad (2)$$

assuming that  $n_1=1.0$  (air).

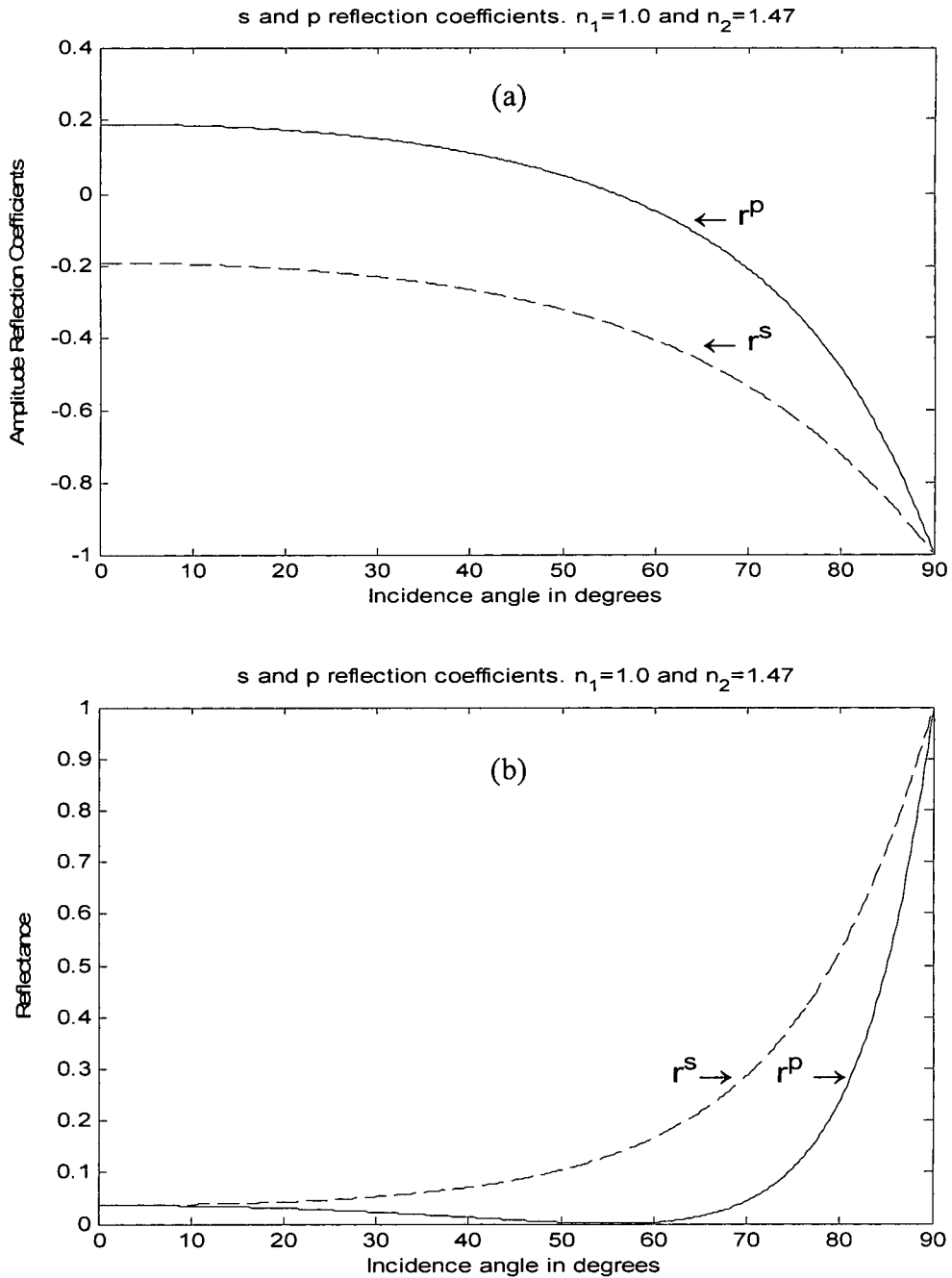


Figure 3. s and p reflection coefficients vs. incidence angle: amplitudes (a); power (b). The power reflection coefficients are magnitude square of the amplitude reflection coefficients.

Figure 3 above shows the plots of the amplitude reflection coefficients and their corresponding reflectances for several incidence angles, assuming values of  $n_1 = 1.0$  (air) and  $n_2 = 1.47$ . Note that the p polarization reflectivity goes to zero at the Brewster's angle, in this case the angle is  $55.77^\circ$ . At the Brewster's angle only the s polarization is reflected, and this is why this angle is also known as the "polarizing angle" [2]. When the angle of incidence is 90 degrees the amplitude reflection coefficients and their reflectances become equal.

### **B. Multiple Reflections on a Multi-layered Medium**

In the case of a layered medium (example: a thin film deposited on a substrate), the laws of reflection are still the same as in the case of the single interface treated above, except that the reflection law needs to be applied on each interface. Figure 4 shows the setup of a simple case of two interfaces, i.e one medium on top of another. In ellipsometry the first medium is usually a thin film of some sort deposited on a second medium often referred to as "substrate". The first interface is between the

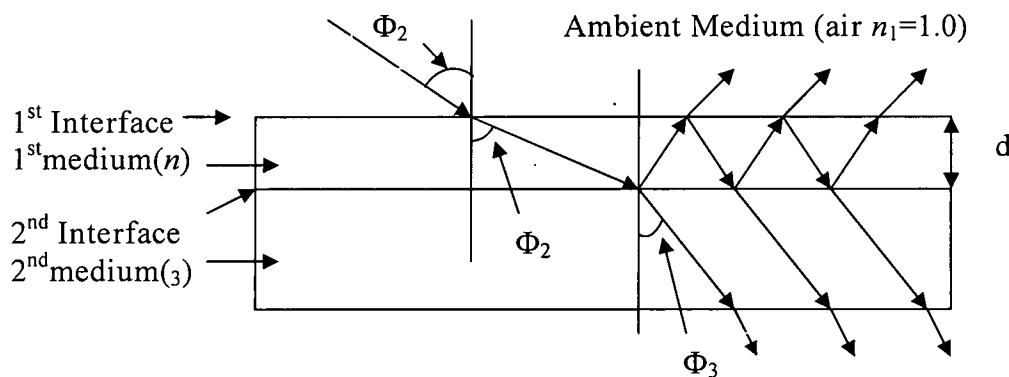


Figure 4. Multiple reflections at a multi-layered medium interfaces.

ambient medium (usually air) and the first medium, and the second interface is between the first medium and the substrate.



The Fresnel coefficients for both p and s polarizations in the case of a multilayered medium are given by

$$r^p = \frac{r_{12}^p + r_{23}^p \exp(-j2\beta)}{1 + r_{12}^p r_{23}^p \exp(-j2\beta)}, \quad r^s = \frac{r_{12}^s + r_{23}^s \exp(-j2\beta)}{1 + r_{12}^s r_{23}^s \exp(-j2\beta)} \quad (3)$$

where  $r_{12}^p$ ,  $r_{23}^p$ ,  $r_{12}^s$ ,  $r_{23}^s$ , are the Fresnel coefficients for p and s polarizations at the first and second interfaces, respectively.  $\beta$  is the phase accumulated by a ray traveling from the first interface to the second interface and back up to the first interface. It is defined as

$$\beta = 2\pi \frac{d}{\lambda_0} n_2 \cos \Phi_2 \quad (4)$$

where  $d$  is the thickness of the first medium and  $\lambda_0$  is the wavelength of the incident field in the vacuum. Most introductory optics and physics text books such as reference (1) usually treats the subject of reflection with much more details.

### C. Ellipsometric Definitions

Referring to figure 1, the phase difference between the incoming s polarization and the p polarization is defined as  $\delta_1$ , and that between the outgoing s and p components as  $\delta_2$ . Further, another parameter  $\Delta$  is defined as

$$\Delta = \delta_1 - \delta_2 \quad (5)$$

As defined,  $\Delta$  is the change in phase difference between s and p that occurs upon reflection and its value can vary from  $0^\circ$  to  $360^\circ$ . It is necessary to keep in mind that the amplitude of both s and p polarization may change upon reflection, without regard to the phase.  $r^s$  and  $r^p$  from equations (3) are the ratios of the amplitudes of reflected s and p polarizations to those of incident s and p polarizations. Using  $r^s$  and  $r^p$  a quantity  $\Psi$  can be defined such that

$$\tan \Psi = \frac{|r^p|}{|r^s|}. \quad (6)$$

The quantity  $\Psi$  is an angle (free to vary from  $0^\circ$  and  $360^\circ$ ) whose tangent is the ratio of the magnitudes of the total s and p reflection coefficients given in equations (3). Furthermore, a complex quantity  $\rho$  can be defined to be the ratio of the total reflection coefficients such that

$$\rho = \frac{r^p}{r^s}. \quad (7)$$

Equations 3 – 7 help define the fundamental equation of ellipsometry in the form given below in equation (8). This equation forms the essence of ellipsometry in that the dynamics of polarization change on reflection are fully described and accounted for by its parameters.

$$\rho = \frac{r^p}{r^s} = \tan \Psi e^{j\Delta} \quad (8)$$

An ellipsometer measures the quantities  $\Psi$  and  $\Delta$ . To be able to deduce the thickness and the refractive index of a sample one needs to construct an optical model of the sample. The model parameters and the  $(\Psi, \Delta)$  data can be utilized in an iterative regression algorithm that minimizes the error between the model's prediction and the measured data by repetitively adjusting the model's parameters until a convergence is reached. Whether the result converges quickly depends mainly on whether the assumed model is correct, although the type of regression algorithm used does influence the convergence to some extent.

## CHAPTER I

### THE BASICS OF ELLIPSOMETRY

#### **A. Brief Historical Background.**

The history of measuring polarization change upon reflection dates back in the late 1800s, although it was not referred to as “ellipsometry” then [3]. The technique of ellipsometry as such is conventionally attributed to Paul Drude who used it to determine the dielectric function of various metals and dielectrics. For 75 years following Drude's pioneering work, only a handful of ellipsometric studies were carried out. The name “ellipsometry” was introduced in 1945 in an article published in *Review of Scientific Instruments* by Alexander Rothen [3]. With the coming of the computer in the late 1960's ellipsometry has gone through a major revolution in that ellipsometric data collection and processing is no longer a daunting task it once was. Of particular interest is how the technique has become the standard in the semiconductor industry for characterization of thin-films and microchips in the visible, NIR, and UV regions.

Among many parameters that ellipsometry measures, the thickness and the refractive index of a sample are the most common. Existing ellipsometric techniques are capable of producing a sample's image and surface topography. Ellipsometry directly measures two parameters,  $\psi$  and  $\Delta$ , which are defined in equation (8). Once the  $(\Psi, \Delta)$  pairs are measured, an optical model of the sample and the

experimentally measured data can be used in a regression algorithm to extract the thickness and the refractive index among other characteristic properties of the sample under examination. Therefore a complete ellipsometric measurement process consist of two major steps: data collection (instrumentation and measurement), and data processing (computation).

### **B. Common Optical Elements Used in Ellipsometry.**

The basic instrumentation of ellipsometry usually requires the following optical elements:

- A light source. A monochromatic light source is usually used for fixed wavelength ellipsometry. A basic research ellipsometer can use a Helium-Neon laser with a wavelength of 633 nm for illumination. Spectroscopic ellipsometry requires the use of a broad spectral band source.
- A polarizer. This component produces light in a special state of polarization. A linear polarizer works by suppressing or redirecting one component of the incident polarization, thus allowing only the other component to pass through. By rotating such a polarizer, one may produce a beam of linearly polarized light from unpolarized incident light a, with the direction of polarization corresponding to the orientation of the transmission axis of the polarizer.
- An analyzer (this is usually another polarizer) to help determine the state of polarization of the reflected beam. Usually the incident beam is already polarized and the analyzer measures the ratio of the p- and the s-polarization

components. A good analyzer would transmit light only along its transmission axes, thus allowing no light to leak that is polarized orthogonally with respect to the transmission axis.

- A detector to measure the irradiance of the light being reflected from the sample. A detector with a wide active area is preferred in ellipsometry for an efficient collection of light. The source wavelength must always fall within the operating spectral range of the detector.
- A computation capability to process the data and interpret the results (this can be a computer that automates the entire system, i.e. controls various devices, collects the data and analyzes it).

Advanced ellipsometric configurations usually use other elements such as quarter-wave plates (QWP), half-wave plates (HWP), electro-optic modulators, and beam splitters to perform various tasks in the instrument. Quarter-wave and half-wave plates are generally referred to as *retarders* or *compensators* from the fact that they operate on the incident light by introducing phases of  $\frac{\pi}{2}$  and  $\pi$ , respectively, between the polarization components along their fast and slow axes. According to their designs certain ellipsometers may require that the beam in the illumination arm of the instrument be either circularly or elliptically polarized. In such a case one would need to generate the desired illumination polarization by combining a polarizer and a QWP and orienting them appropriately. The polarizer-QWP combination can also be used when analyzing an elliptical polarization. Half-wave plates can be used to manipulate the beam polarization before or after reflection on the sample. For example, two HWP can act as a polarization rotator with the

rotation angle being determined by the angle between the two plates' fast axes [4]. Some recent ellipsometer designs incorporate a modulator of some kind to modulate the ellipsometric signal at relatively high frequencies. The most widely used modulators in ellipsometers are Faraday modulators and photo-elastic modulators (PEM) since they can be modulated at a frequency as high as 100 KHz [5], which is fast enough by ellipsometric standards. Beam splitters are primarily used to steer the beam and can be used where appropriate.

### **C. Common Ellipsometer Arrangements**

Nulling ellipsometry is the most widely used configuration and the research work presented in this thesis is based on implementing a variation of the nulling technique. Most arrangements discussed in this section are nulling ellipsometer arrangements, however a few other arrangements will be discussed as well. These arrangements only represent the conceptual models since in practice modifications are always introduced to implement functional systems. The nulling technique advantage resides in its working principle, i.e. the determination of the reflected polarization by simply determining the angles of the polarizer, the analyzer, and the compensator that result into a null. Photometric ellipsometry and interferometric ellipsometry, for example, rely on the intensity of light in order to determine the reflected polarization and therefore are subject to the signal-to-noise ratio penalty due to the intensity fluctuations. By simply detecting a null (zero intensity) and then determining the reflected polarization using the geometry of the setup which produced the null, the measurements are not affected as much by the intensity

fluctuations. This is a major advantage that the nulling technique offers. In addition, it is easier to accurately measure a null than it is to accurately measure a nonzero intensity. In this regard too the nulling technique offers an advantage.

### **C.1 Nulling Ellipsometer**

The manual nulling scheme was the first method used to measure polarization change upon reflection. Few nulling ellipsometric setups are explored below in order to understand the basic functioning principle of a nulling instrument.

Conceptually a nulling ellipsometer is a simple system that uses a polarizer, an analyzer, a quarter-wave plate (QWP), and a detector (or screen) to detect the presence of a null (zero irradiance at the detector) [3]. One conceptual ellipsometer is shown in figure 5. Unpolarized light from the source goes through the polarizer (P) and becomes linearly polarized in the direction of the polarizer's transmission axis. On the sample (S) the incident linear polarization picks up an amount of ellipticity and becomes elliptically polarized. This elliptical polarization is converted

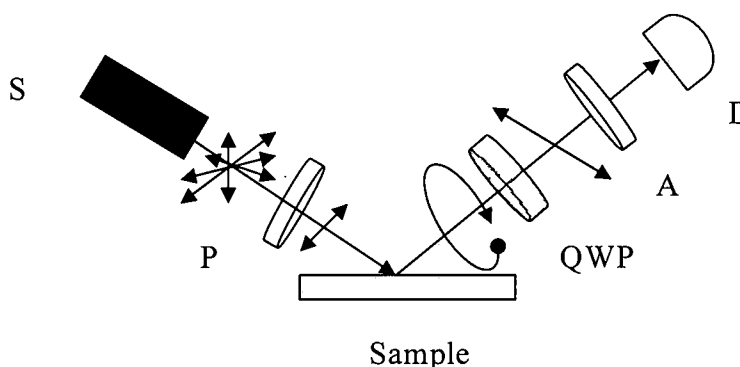


Figure 5. A conceptual nulling ellipsometer arrangement :  
S: source (laser); P: polarizer; QWP: quarter-wave plate;  
A: analyzer; D: detector.

into linear polarization by properly adjusting the QWP angle. The linear polarization emerging from the plate can be easily nulled by adjusting the analyzer (A) angle. Note that if the quarter-wave plate angle is not properly adjusted a minimum, not a null, will be found. In practice, the QWP is usually placed right after the polarizer as shown in figure 6. Generally the combination of a polarizer and a quarter-wave plate behaves as an elliptical polarizer. The ellipticity can be adjusted by changing the angle between the two elements' transmission axes so that the ellipticity is totally cancelled (compensated for by the QWP) upon reflection. When such a condition is reached the reflected light is linearly polarized. In the setup illustrated in figure 5 the quarter-wave plate is fixed at 45 degrees. The null is found by iteratively adjusting the polarizer and the analyzer angles. Note that there will be several combinations of the analyzer-polarizer angles that will result in a null. Usually angles are considered positive in the counterclockwise direction when

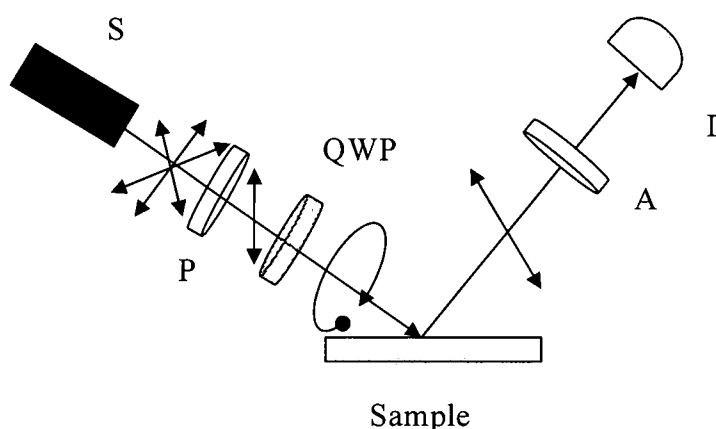


Figure. 6. A conceptual nulling arrangement with the QWP inserted before the sample.

when looking into the beam. If the polarizer's angle  $P$  and the analyzer's angle  $A$  are restricted to certain ranges to avoid redundant angles (angles  $180^\circ$  apart), then



the various combinations of P and A that result in a null can be grouped into two zones [3] as follows:

$$\text{Zone 2: } -45^\circ < P_2 < 135^\circ, \quad 0^\circ < A_2 < 90^\circ, \text{ QWP} = 45^\circ \quad (9)$$

$$\text{Zone 4: } -135^\circ < P_4 < 45^\circ, \quad -90^\circ < A_4 < 0^\circ, \text{ QWP} = 45^\circ. \quad (10)$$

The ellipsometric parameters  $\Delta$  and  $\Psi$ , as defined earlier are related as follows:

$$\Delta_2 = 270^\circ - P_2, \quad \Delta_4 = 90^\circ - 2P_4 \quad (11)$$

$$\Psi_2 = A_2, \quad \Psi_4 = -A_4. \quad (12)$$

More details on equations (9) through (12) can be found in reference [3]. Figure 7 illustrates the detected intensity plot near a null. The change in intensity as a function of the polarizer's angle is very small near the null point. Since the intensity curve is symmetric (for the case in figure 6) with respect to the null position (see figure 7), a better way of measuring the exact null position may be to measure two angular positions that give equal intensities (near the apparent null) one from each side of the curve and divide the sum of the angles by two.

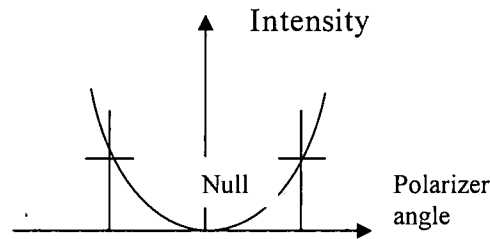


Figure. 7 Intensity vs. polarizer's angle near the null.

## C.2 The Rotating Elements Ellipsometer

A rotating ellipsometer automatically rotates its polarizer and analyzer to find a null position. Figure 8 illustrates a setup of a rotating elements ellipsometer. Unlike

in figure 6 the polarizer in figure 8 is not fixed. It is rotated simultaneously with the analyzer. For a rotating elements ellipsometer the signal on the photodetector is a sinusoidal varying intensity. Generally the minima of this intensity do not correspond to the intensity extinction (null), i.e. the intensity does not go to zero. These minima deepen and eventually go to zero when the polarizer and the analyzer are alternatively adjusted to find a proper combination of their angular positions that leads to a null. With the advent of high precision electronics the search for these angles is often done by microprocessor-driven servomotors that control and encode the angular positions of the polarizer and the analyzer. The encoded polarizer and analyzer angles corresponding to the null occurrences are used to calculate the values of  $\Delta$  and  $\Psi$ . The QWP is inserted with its fast axis perpendicular to the plane of incidence and can be placed in the beam or removed from it. With the polarizer

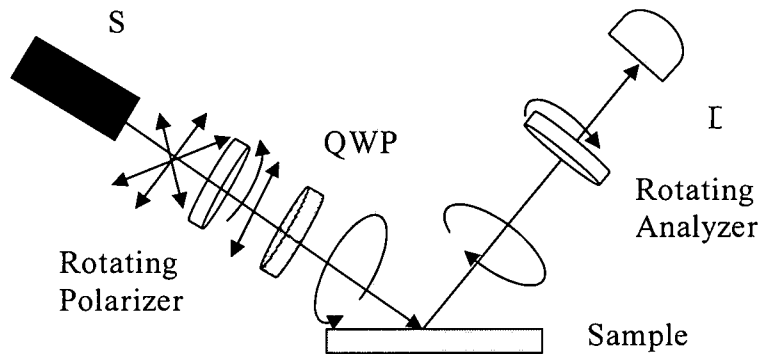


Figure 8. A rotating null ellipsometer arrangement.

fixed at an angle the arrangement becomes a photometric instrument instead of a null instrument. Its signal [3] is sinusoidal and is given by

$$I(t) = I_0 [1 + \alpha \cos 2A(t) + \beta \sin 2A(t)], \quad (13)$$

where

$$A(t) = 2\pi f t + A_c \quad (14)$$

with  $A(t)$  being the time varying analyzer angle,  $f$  being the frequency of the rotation and  $A_c$  being a constant angle offset.  $I_0$  is the average intensity and  $\alpha$  and  $\beta$  are Fourier coefficients (to be calculated).  $\Psi$  and  $\Delta$  are found using the following relationships [3]

$$\cos \Delta = \pm \sqrt{\frac{\beta^2}{1 - \alpha^2}}, \quad (15)$$

$$\tan \Psi = \sqrt{\frac{1 + \alpha}{1 - \alpha}}. \quad (16)$$

A more realistic rotating null ellipsometer setup can be seen in figure 9 [6]. This configuration is more advanced and beyond a simple conceptual model. The first arm contains a source, a polarizer, and a compensator while the second arm contains a motor that controls and encode the analyzer angle, the analyzer itself, and a detector. The system extends outside where signal amplification, conditioning, and processing are done using an analogue-to-digital (A/D) converter and a computer. Assuming that the second analyzer (fixed analyzer A) is removed, this arrangement becomes basically a variation of the rotating analyzer configuration already mentioned above. The basic optical elements are arranged from light source to detector as follows: polarizer – compensator – sample – analyzer. This arrangement order is often referred to as PCSA arrangement. The signal received at the detector, as shown in the diagram, shows that a null in the irradiance can be produced given an appropriate polarizer-compensator-analyzer angular combination when analyzer  $A_r$  is removed from the analyzer arm. The automation of this instrument increases the accuracy with which the measurements are taken,

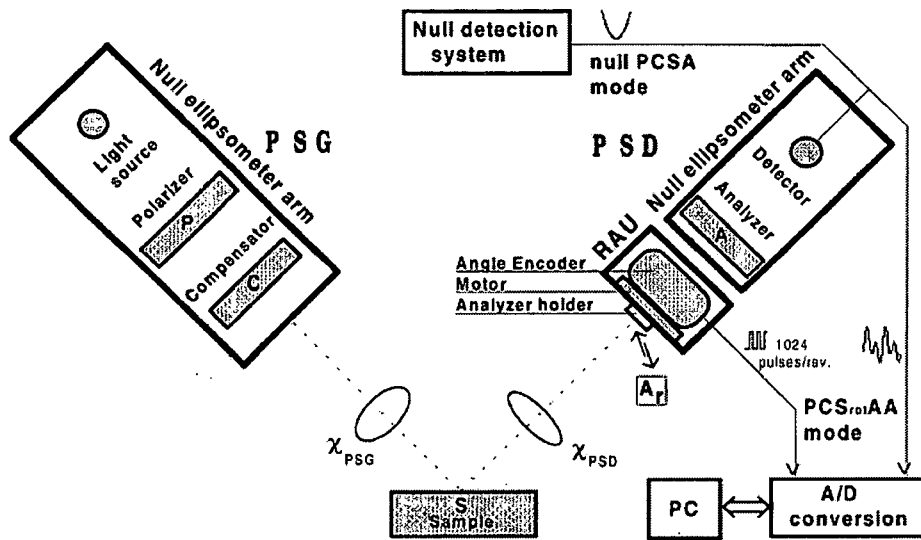


Figure 9. Rotating null ellipsometer (figure published in reference [5]).  $A_r$ : rotating analyzer; A: non-rotating analyzer.

and allows a fast collection of data. On the other side, the different optical and electronic components involved may increase the complexity of the instrumentation and the calibration.

### C.3 The PSRA Ellipsometer

The acronym PSRA stands for Polarizer, Sample, Rotator, and Analyzer. It tells the order in which the elements appear in the setup from light source to detector. Figure 10 illustrates the configuration of this arrangement. This setup is also known as the “Monin - Boutry” ellipsometer [1]. The beam from the source is linearly polarized and directed toward the sample. After reflection on the sample the light picks up a phase and becomes elliptically polarize. The elliptically polarized light enters a polarization rotator (Faraday rotator) which is driven by an ac current of frequency  $\omega$  through a coil. A is a linear analyzer and D is a detector. This type of

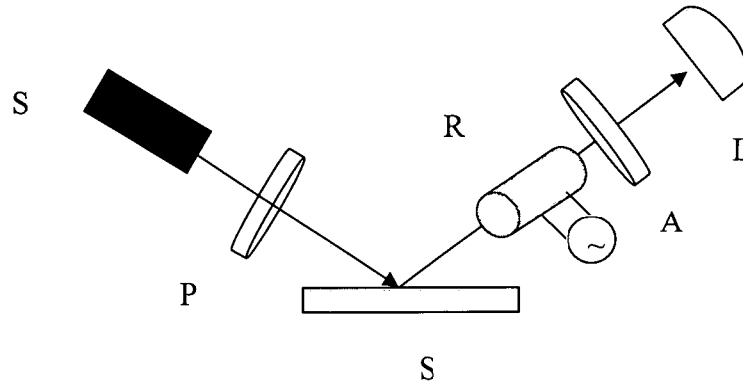


Figure 10. PSRA ellipsometer basic arrangement.

ellipsometer functions based on the principle that when the transmission axis of the linear analyzer is oriented parallel to either the major or the minor axis of the ellipse of polarization of the reflected light the detected signal will have a zero-amplitude harmonic at the modulation frequency. This means that with the polarizer set at a fixed azimuth the analyzer can be rotated until the signal component at  $\omega$  is nulled. The driving current in the coil generates a magnetic field given by

$$H(t) = H_m \cos \omega_0 t \quad (17)$$

where  $H_m$  is the field amplitude and  $\omega_0$  is the frequency of the driving current. Using  $\nu$  as the Verdet constant,  $L$  as the length of the Faraday cell, and  $\omega$  as the driving current frequency the modulation function of the rotator can be written as [7]

$$\Phi = \nu L H_m \cos \omega_0 t = \Phi_m \cos \omega_0 t \quad (18)$$

At the output of the modulator the electric field vibrations are given by

$$E_x = a \cos \omega_0 t \cos \Phi + b \sin \omega_0 t \sin \Phi \quad (19)$$

$$E_y = -a \cos \omega_0 t \sin \Phi + b \sin \omega_0 t \cos \Phi \quad (20)$$

where  $a$  and  $b$  are the incident polarization ellipse major and minor axes, respectively. If the analyzer angle is  $\beta$  and the orientation of the ellipse is  $\theta_0$  then the general form of the signal [7] on the detector is given by

$$I = a^2 \cos^2 (\Phi + \beta - \theta_0) + b^2 \sin^2 (\alpha + \beta - \theta_0). \quad (21)$$

Assuming  $\Phi_m \ll 1$ , the signal can be expanded as a Taylor series. The harmonic components that results from the expansion are given as follows [7],

$$I(0) = \frac{b^2}{\varepsilon^2} \left[ \cos^2 (\beta - \theta_0) + \frac{\Phi_m^2}{2} \cos^2 2(\beta - \theta_0) \right] + a^2 \varepsilon^2 \left[ \sin^2 (\beta - \theta_0) + \frac{\Phi_m^2}{2} \cos^2 2(\beta - \theta_0) \right] \quad (22)$$

(d.c component) ,

$$I(\omega_0) = K_1 a^2 (\varepsilon^2 - 1) \sin^2 2(\beta - \theta_0) \cos \omega_0 t \quad (\text{first harmonic}), \quad (23)$$

$$I(2\omega_0) = K_2 a^2 (\varepsilon^2 - 1) \cos 2(\beta - \theta_0) \cos 2\omega_0 t \quad (\text{second harmonic}), \quad (24)$$

where  $K_1$  and  $K_2$  are the constants proportional to  $\Phi_m$ , and  $\varepsilon$  is the ellipticity angle of the polarization after reflection. Note that for  $\beta = \theta_0$  or  $\beta = \theta_0 \pm \pi/2$  the first harmonic disappears and a null occurs.

Besides the ellipsometers mentioned above there are many types of ellipsometers including polarization modulation ellipsometers (PME), interferometric ellipsometer (IE), etc. But they are beyond the scope this work. Details on these ellipsometers can be found in reference [2].

## **CHAPTER II**

### **NEW DEVELOPMENTS AND ISSUES IN ELLIPSOMETRY**

Many significant developments have been reported in the attempt to improve the general ellipsometric performance. Many methods have been devised in the quest for better spatial resolution, higher signal-to-noise ratio (SNR), more precise measurements, and faster data collection and processing. With respect to improving the spatial resolution M. Erman and J.B. Tetheon proposed the use of a convergent beam combined with a high numerical aperture (N.A) objective [8]. The drawback of this approach is that the incident angle is not well defined since both the illumination and the analyzer beams consist of a range of angles defined by the numerical aperture. This often results in poor ellipsometric performance when a high N.A objective is used. Another problem is that a high N.A, i.e. high spatial resolution would require a very short working distance of the objective which can lead to the risk of crashing the objective into the sample. An image scanning method based on nulling ellipsometry was proposed by An-Hong et. al. [9]. It was claimed that an instrument based on this method would be capable of achieving high spatial resolution and high surface sensitivity while generating a 2-D map of the sample thickness. More recently another approach termed back focal plane ellipsometry using a large NA lens for high spatial resolution was demonstrated [10]. The reflected s and p polarizations coming from the sample are collected by the objective

and analyzed in the back focal plane using a two-detector array. Since the fields at the back and front focal planes relate to each other through a Fourier transform, each incidence angle is mapped to a specific location in the back focal plane. The signal-to-noise ratio of such an instrument depends on the detector's pixel size, and that becomes a problem when using a small pixel size since the trade off would be a lower signal-to-noise ratio. A comparative study of several other methods can be found in reference [11].

With the feature sizes of new electronic and optoelectronic devices shrinking from microscale to nanoscale the resolution of commercially available ellipsometers has been stretched to its limit. According to the International Roadmap for Semiconductors (ITRS) [12], key areas of metrology that would require solutions in the several years are:

- Characterization of devices built on new types of substrates such as SiGe and strained silicon layers.
- Non-destructive microscopy for measuring and analyzing 3D structures and detecting defects in semiconductors.
- Metrology of gate dielectric thin films.

Most of these technical challenges involve the need for higher spatial resolution metrology of thin films thickness and refractive index. The existing ellipsometric and non-ellipsometric capabilities have been able to cope with these issues to some extent, but it is unlikely that the roadmap specifications will be met if new and improved capabilities are not available soon. In this work I will discuss a high resolution nulling ellipsometer based on a rotational polarization symmetry concept.



This microellipsometer is one of the many proposed solutions that are still being researched in order to respond to the new metrology challenges. Compared with other microellipsometers our instrument provides an improved resolution and a higher SNR, in addition to faster and precise automated measurements and data processing. However due to the scope of this work we will not be able to present measurements of optical properties such as thickness and refractive index. Instead, sets of raw preliminary data will be presented and discussed to demonstrate the basic principle of our design.

## CHAPTER III

### DESIGN OF A RADIALLY SYMMETRIC MICROELLIPSOMETER

#### A. Fundamentals of the Design

To address the issues of low spatial resolution and low signal-to-noise ratio present in many ellipsometers a new microellipsometer that uses a high numerical aperture objective for wide angle illumination and high spatial resolution has been designed [4], built, and tested. The design is based on the rotational symmetry of the polarization in the signal. The design concept is illustrated in figure 11. Figure 11(a) shows a conventional ellipsometer. A linear polarization illuminating the sample picks up an amount of ellipticity on reflection and becomes elliptically polarized. In figure 11(b) a high NA lens is inserted so that the ray is tightly focused into a small spot on the sample. A single ray, as shown, can be regarded simply as one channel in

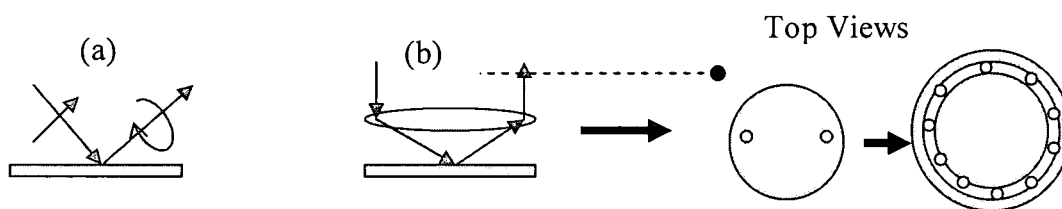


Figure. 11 (a) A standard ellipsometer (b) After a high NA lens insertion.

the pupil plan of the objective lens. In order to obtain a radial symmetry the single ray in figure 11(b) needs to be *exactly* and *symmetrically* reproduced with respect to the optical axis of the lens as shown in the top view of figure 11(b). This is not an

easy task to accomplish. Multiple channels symmetrically arranged around the optical axis form multiple channels each carrying an *identical* signal polarization illuminating the sample. Note that this is not a simple geometrical symmetry; it's a polarization symmetry.

The concept discussed above can be realized in a minimal conceptual ellipsometric configuration shown in figure 12. An incident linearly polarized beam is converted into a circularly polarized beam by properly adjusting the angle between the polarizer and the quarter-wave plate. This angle must be adjusted so that the polarization coming out the first beam-splitter and illuminating the objective is circular. At that point the polarization distortion caused by imperfections in the beam-splitter would be compensated for. The back focal plane

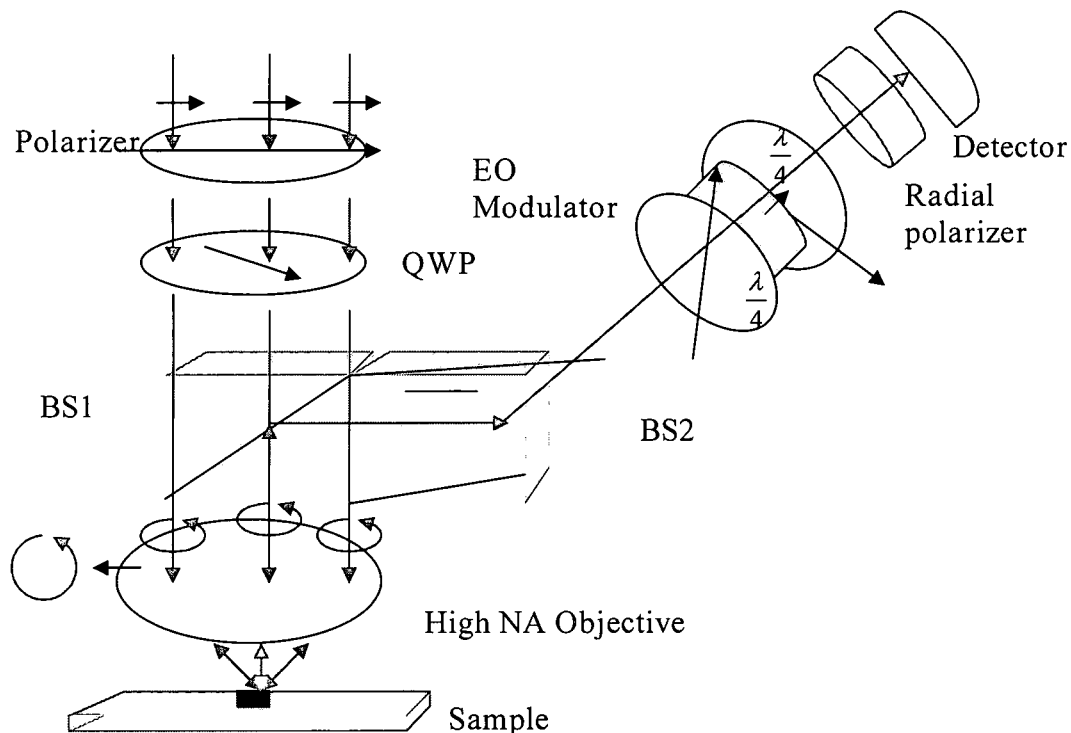


Figure 12. Conceptual diagram of radially symmetric microellipsometer design. BS1: first beam splitter; BS2: second beam splitter.

is illuminated by symmetric channels of circularly polarized light, and each channel *identically* contributes to the total signal. This collaboration among individual channels significantly improves the overall signal-to-noise ratio of the system. The only difference among channels is a geometric phase due to the physical location of each channel in the objective's pupil. This phase is commonly known as Berry's phase [13] and does not affect the signal since the detector only responds to the signal power. A high N.A allows high angle illumination and focuses the circularly polarized beam down to a small spot on the sample, and collects the reflected light. The high angle illumination also gives a better ellipsometric signal level. The small spot size is the basis for spatial resolution improvement. The circular polarization incident on the sample picks up a phase and an amplitude upon reflection and generally becomes elliptically polarized. So far the symmetry in the polarization is maintained. Two identical beam-splitters are used in this design for two purposes: beam steering and conservation of polarization symmetry [4]. The first beam-splitter, just as most beam-splitters, has different responses to p and s polarizations. This difference in polarization responses causes polarization distortions and ultimately destroys the polarization symmetry. To solve this problem a second beam-splitter that is *identical to the first beam splitter* is inserted and positioned as shown in figure 12 such that the s-polarization for the first beam-splitter becomes the p-polarization for the second beam-splitter and vice versa. This arrangement allows both s- and p-polarization to be affected the same way and thus, the

polarization symmetry is maintained as the beam is being directed towards the analyzer arm of the ellipsometer.

The analyzer arm uses an electro-optic modulator consisting of two quarter-wave plates and a variable electro-optic retarder as shown in figure 13. Note that the two QWPs axes are orthogonal and the crystal axis must be positioned at  $45^\circ$  between the two quarter-wave plates fast axes. When configured as such the transmission Jones matrix of the total device is a rotation matrix [14]. This device acts like a *pure*

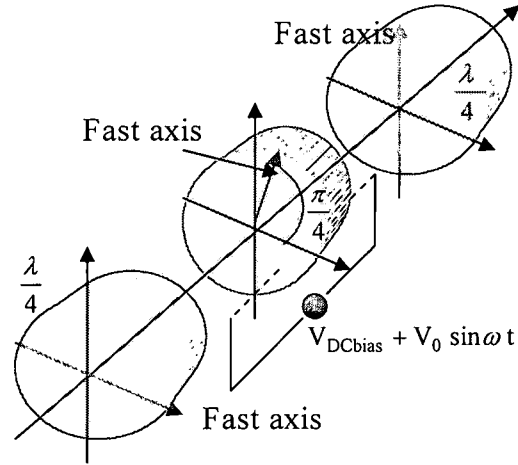


Figure 13. Diagram of the EO circular variable

*polarization rotator* and the phase factor has no effect here since only the signal power is being detected. The Jones matrix of the device is given by

$$T = \overbrace{R(-\frac{\pi}{2})}^{\text{Second QWP}} \overbrace{\begin{pmatrix} 1 & 0 \\ 0 & -j \end{pmatrix}}^{\text{EO retarder}} \overbrace{R(\frac{\pi}{2})}^{\text{First QWP}} \overbrace{\begin{pmatrix} 1 & 0 \\ 0 & -j \end{pmatrix}}^{\text{Phase factor}} = -je^{-j\frac{\delta}{2}} R(\frac{\delta}{2}). \quad (25)$$

where  $\delta$  is the retardation from the variable retarder. This retardation depends on the voltage applied to the electro-optic crystal and the wavelength. This relationship

is given by

$$\delta = \frac{2\pi}{\lambda_0} n_0^3 r_{63} V \quad (26)$$

where  $n_0$  and  $r_{63}$  are the ordinary refractive index and the electro-optic coefficient of the crystal, respectively, and  $V$  is the voltage applied across the crystal. It is important to note that this is a polarization rotation operation independent of the initial state of polarization. The rotation angle is determined only by the retardation produced by the crystal which, in turn, depends on the applied voltage.

For purpose of detection the rotation angle produced by the applied voltage is a d.c bias modulated by a small high frequency a.c component so that the total rotation angle (which is variable) at any time is the sum of the two contributions. This device can be modulated at several KHz up to 1 MHz [14]. This leads to higher polarization rotation frequencies, a shorter integration time for lock-in detection, and faster scanning of samples. Most importantly, this device allows the implementation of the nulling technique in this design. The elliptical polarization generated by the circular polarization reflection on the sample enters the polarization rotator. The biasing action makes it that every ellipse of polarization in each channel is locally rotated by the *same amount proportionally to the applied voltage*. As in the case of the PSRA ellipsometric arrangement described in chapter one, *when these polarization ellipses are rotated such that one of their axes becomes parallel to the analyzer transmission axis, a null first of the first harmonic component will be observed* in the detected signal. The nature of the signal and the null will be explored in the next section and later in chapter four.

## B. Signal Derivation and Nulling Scheme Implementation

The total signal on the detector can be derived using Jones calculus [4]. The derivation is based on the geometric layout of the contributing channels in the pupil plane as shown in figure 14. In this diagram the illuminating wave is a circularly polarized plane wave in the  $xOy$  coordinate system (this is the laboratory coordinate) and its Jones matrix is given by  $E_{in} = \begin{pmatrix} 1 \\ j \end{pmatrix}$ . Suppose a ray is entering the pupil at an azimuthal angle  $\varphi$ . As said before, this ray can be treated as a single channel. The coordinate system of this channel is  $x_iOy_i$  (this is the local coordinate system), as shown in figure 14. This coordinate system was chosen such that the two

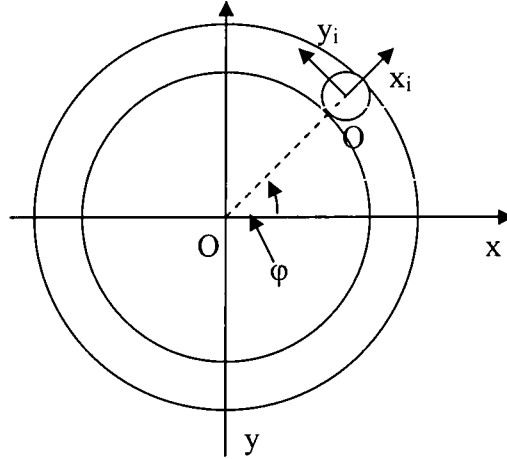


Figure 14. Coordinate systems used for signal derivation.

eigenvectors align with the s and p directions when the ray hits the sample. In the local coordinate system the incident polarization is

$$E_{loc} = R(\varphi)E_{in} = \begin{pmatrix} \cos \varphi & \sin \varphi \\ -\sin \varphi & \cos \varphi \end{pmatrix} \begin{pmatrix} 1 \\ j \end{pmatrix} = e^{j\varphi} \begin{pmatrix} 1 \\ j \end{pmatrix}. \quad (27)$$

Equation (27) shows that each local channel sees a circularly polarized light with a phase shift. This phase shift is the Berry's phase that we mentioned earlier, which is geometric in nature. After reflection on the sample the circular polarization will pick up an amount of ellipticity, and depending on the sample being examined this polarization will generally become elliptically polarized. Because of the radial symmetry, each channel will carry an identical elliptical state of polarization, except for the geometrical phase. Let's suppose that in each local channel there is an ellipse of polarization with ellipticity angle  $\varepsilon$  and semi-longitudinal axis making an angle  $\theta_0$  with respect to  $Ox_i$ . When the d.c and a.c voltage biases are applied across the modulator the polarization rotation introduced by the variable retarder is

$$\Phi = \Phi_{bias} + \alpha_m \cos \omega t \quad (28)$$

where  $\Phi_{bias}$  is controlled by the d.c voltage and  $\alpha_m$  is the modulation amplitude of the rotation angle due to the a.c voltage component. Equation (28) is similar in function to equation (18) relative to the Monin-Boutry ellipsometer [7] discussed in chapter one although in that case the modulation is based on the magnetic field produced by a current-driven coil. The general form of the signal is identical to that of a rotating analyzer ellipsometer [3]. In our case the general signal can then be written as

$$P = K \{1 + \cos 2\varepsilon \cos[2(\Phi_{bias} + \alpha_m \cos \omega t + \theta_0)]\}. \quad (29)$$

As in the case of the PSRA ellipsometer in chapter one, assuming a small angular modulation, i.e.  $\alpha_m \ll 1$  and using Taylor's expansion rule, the cosine term in equation (29) can be expanded [10] as follows



$$\begin{aligned} & \cos[2(\Phi_{bias} + \alpha_m \cos \omega t + \theta_0)] \\ & \cong \cos 2(\Phi_{bias} + \theta_0) (1 - \alpha_m^2 + \alpha_m^2 \cos 2\omega t) - 2\alpha_m \sin 2(\Phi_{bias} + \theta_0) \cos \omega t \end{aligned} \quad (30)$$

The substitution of equation (30) into equation (29) reveals that the general signal is made up of the following harmonic components [4]:

$$P(0) = K [1 + \cos 2\varepsilon (1 - \alpha_m^2) \cos 2(\Phi_{bias} + \theta_0)] \quad (31)$$

$$P(\omega) = 2K\alpha_m \cos 2\varepsilon \sin 2(\Phi_{bias} + \theta_0) \cos(\omega t + \pi) \quad (32)$$

$$P(2\omega) = K \cos 2\varepsilon \alpha_m^2 \cos 2(\Phi_{bias} + \theta_0) \cos 2\omega t \quad (33)$$

Equations (31) – (33) bear close similarities to equations (22) – (24). They depend on the ellipticity angle  $\varepsilon$ , the modulation amplitude  $\alpha_m$ , and the ellipse orientation  $\theta_0$ , among other parameters. Similarly to equation (23), it can be deduced from equation (32) that when  $\Phi_{bias} = -\theta_0$  or  $\Phi_{bias} = -\theta_0 \pm \frac{\pi}{2}$  the first harmonic becomes *null*, i.e.  $P(\omega) = 0$ . The ratio of the d.c signal at two null positions, i.e. at  $\Phi_{bias} = -\theta_0$  and  $\Phi_{bias} = -\theta_0 \pm \frac{\pi}{2}$ , gives  $\tan^2 \varepsilon$ . This means that by adjusting the voltage across the crystal and detecting two consecutive nulls of the first harmonic one can measure the elevation angle  $\theta_0$ , and using the ratio of the d.c signal at the two null positions one can determine  $\varepsilon$ . Once the pair  $(\varepsilon, \theta_0)$  is known the pair  $(\Psi, \Delta)$  can in turn be determined. With  $\Psi$  and  $\Delta$  known at each position on the sample, a regression algorithm can be applied to retrieve the properties of the sample. So, the use of a circular variable retarder combined with the polarization symmetry concept, enables the implementation of the *nulling* technique and consequently improves the overall signal-to-noise ratio and the precision of the measurements.

## CHAPTER IV

### INSTRUMENTATION AND TESTING

#### A. Instrumentation

So far the design of our microellipsometer has been explained using partial diagrams addressing individual modules of the instrument. Figure 15 shows the

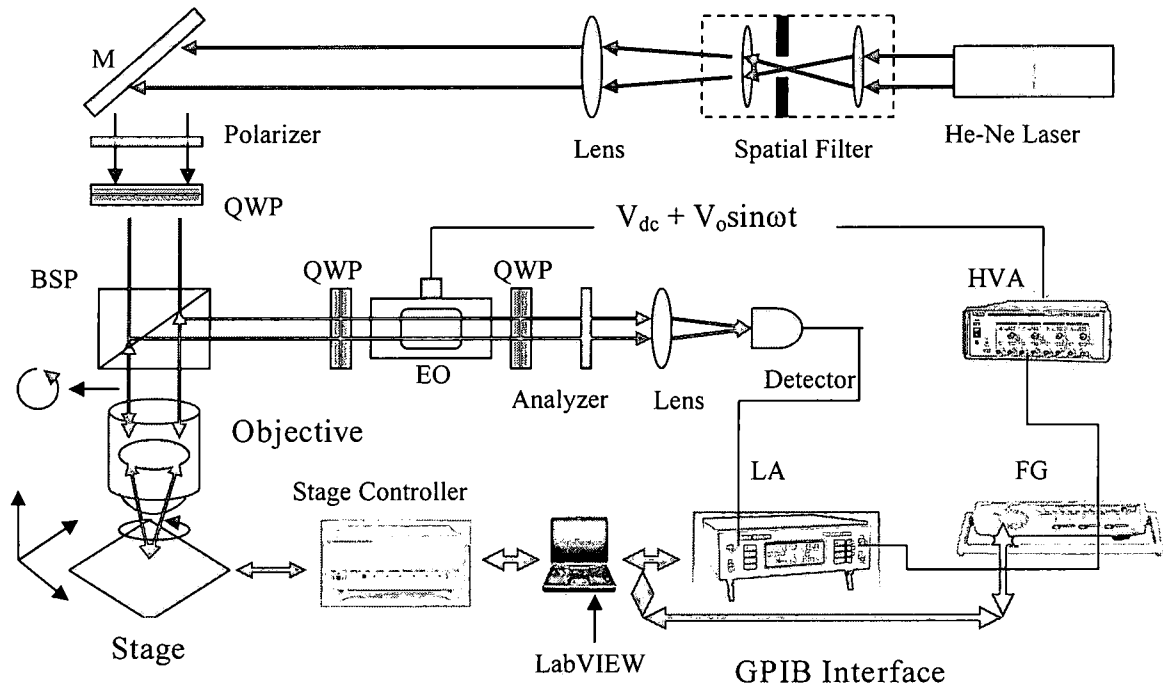


Figure 15. The complete laboratory setup of the microellipsometer. The lockin amplifier (LA) takes the signal and its reference in from the detector and a function generator (FG). The high voltage amplifier (HVA) amplifies (X100) the modulation voltage from the function generator. The amplified modulation voltage is applied across the electro-optic modulator (EO). BSP is the beam splitter pair.

integral laboratory setup of the microellipsometer. The illumination starts at the source (a 12 mW HeNe laser, model R-30993 by Electro-optics inc.), goes through

the intermediary elements for collimation and cleaning, and ends up focused by the objective (100x magnification, 0.95 N.A, and 1 mm working distance by Nikon) on the sample. The sample is placed on a translation stage (model ESA-C by Newport) that is controllable in the x-y-z directions using a GPIB interface (IEEE 488.2). The reflected light is collected by the objective and redirected toward the analyzer arm of the instrument by a double beam splitter, and gets focused on the detector (model DET 110 by Thorlab). A function generator (1 $\mu$ Hz to 20 MHz function/ arbitrary wave form generator. Model 33220A by Agilent Technologies) is used to provide a certain range of d.c voltage bias across the modulator. The same function generator also provides a small amplitude a.c voltage for signal modulation and the reference for lock-in detection. A lock-in amplifier (model DSP Lock-in 7265 by Signal Recovery) was used for lock-in detection. The d.c and a.c voltages are sent to a high voltage amplifier (model AMS – 1B30 by Matsushida) for amplification (100x amplification), since the bias across the crystal may need to be as high as 1 Kilovolt; a voltage that cannot be directly achieved with a function generator (5 volts maximum). The lock-in amplifier is operated in dual harmonic mode. This allows the detection of both the first and the second harmonic amplitudes. The signal phase can be detected although it not used in this design.

The instrument is totally computer-controlled, i.e. the function generator, the stage, and the lock-in amplifier are all controlled by a computer using a LabVIEW via GPIB interface. This brings up the issue of interfacing all the equipments listed above in order to get them to execute their tasks in a repetitively sequential order.

While scanning a sample the ellipsometer must execute the tasks in the following order:

1. Move the sample to a spot (starting location on the sample). This is done by the stage controller.
2. On that particular spot, scan the entire d.c bias. This is the role of the function generator.
3. For every bias point in the bias voltage range, record the amplitude of the first harmonic component of the signal.
4. Analyze the data to determine the minimum amplitude of the first harmonic component and find the corresponding voltage.
5. Move the stage to the next spot on the sample and repeat steps 1 - 4.

The tasks in step 4 are performed internally by the software (LabVIEW) which also displays the result (the minimum amplitude voltage) in a file.

As previously discussed, the ellipsometer control is done at the software level using LabVIEW virtual instruments (VI). A VI is an instrument driver that provides a “friendly” graphical user interface (GUI) for entering instrument control parameters. In our case the equipments had preexisting VIs freely available on the National Instruments website. The task was to integrate these individual VIs into a single VI that controls all three instruments using one user interface. The task was achieved after several modifications and additions, but it still needs to be improved. The software has three loops that handle the main tasks of the instruments. Figure 16 shows the details of the internal execution of the software. The two outer loops incrementally adjust the axes voltages in order to translate the sample in the x-y

directions when scanning several spots on the sample. The number of iterations assigned to these loops determines the number of spots to be scanned in the desired directions. The step distances of the translations as well as the number of iterations can be defined on the front panel of the user interface. Once the two outer loops position the sample, the third loop which is in charge of scanning the d.c bias range starts executing. Its assigned number of iterations determines the number of d.c bias point using an adjustable step voltage. The third loop is also in charge of reading the

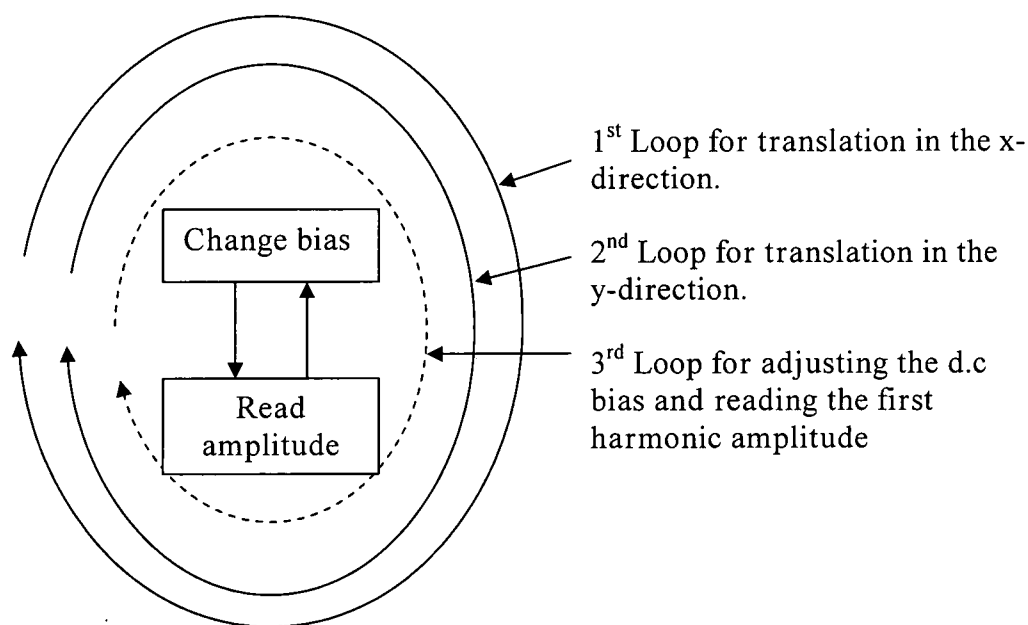


Figure 16. The three loops in charge of instruments control and signal processing.

reading the first harmonic amplitude data from the lock-in amplifier. For every bias amplitude of the signal is read and stored in an array. As mentioned before, for every scanned spot the software uses the amplitude and the voltage data to determine which voltage corresponds to the minimum amplitude of the first harmonic. An algorithm to process the amplitude data for a minimum has been developed and is embedded within the third loop. Once the minimum amplitude

voltages are produced for a certain sample, pairs of  $\theta_0$  and  $\epsilon$  can be obtained. From those pairs corresponding pairs of  $\Psi$  and  $\Delta$  can be obtained.

### **B. Modulator Calibration and System Alignments.**

The calibration of the polarization rotator [14] was done in order to find its rotation coefficient. The setup used for this calibration is shown in figure 17. First the two Polarizers are aligned so that their fast axes are orthogonal. The first QWP is placed between two orthogonal polarizers and the plate is rotated until a null is detected on the detector. Then, the second QWP is introduced and rotated until a null is detected. At this point the two QWPs fast axes are orthogonal. This can be verified by checking that the two position markers on the two QWPs are  $90^\circ$  apart. Next, the modulator is inserted between the two QWPs and a voltage is applied to it. The modulator is then rotated until a null is observed on the detector. At this point the modulator's fast axis is parallel to one of the QWPs fast axis. To place this modulator's fast axis at  $45^\circ$  with respect to each of the QWPs fast axis both QWPs are simultaneously rotated by  $45^\circ$  in the same direction. This step completes the

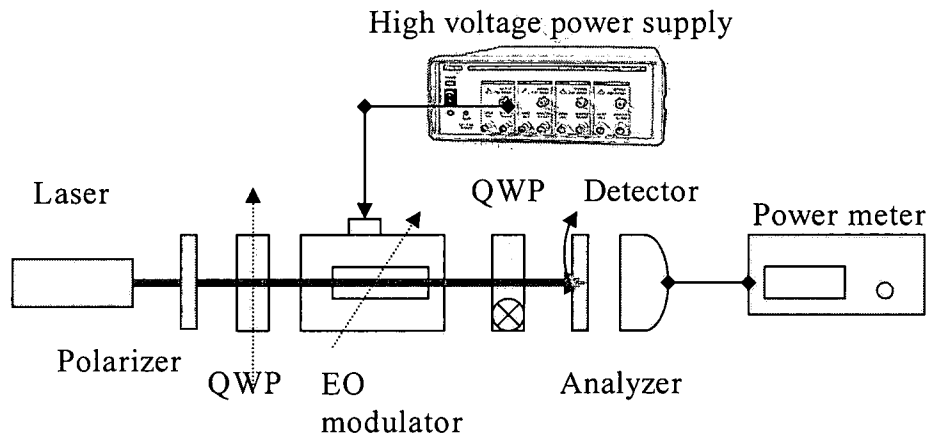


Figure 17. Polarization rotator calibration setup.

alignment of the polarization rotator. The two QWPs and the EO modulator, now, form one unit and behave as a polarization rotator.

The rotator is calibrated by applying a certain range of d.c voltages to the modulator, and for each voltage applied the linear analyzer is rotated to find at which angle of the analyzer a null occurs. For this work a range of d.c bias going from -700 volts to +700 volts was used. The resulting calibration curve was obtained and is shown in figure 18. The equation of line was found to be  $\theta = 0.248 \cdot V + 121.42$ , where  $\theta$  is the rotation angle resulting from a voltage  $V$  applied across the modulator. The rotation coefficient determined from the line equation is  $0.248^\circ/\text{volt}$ .

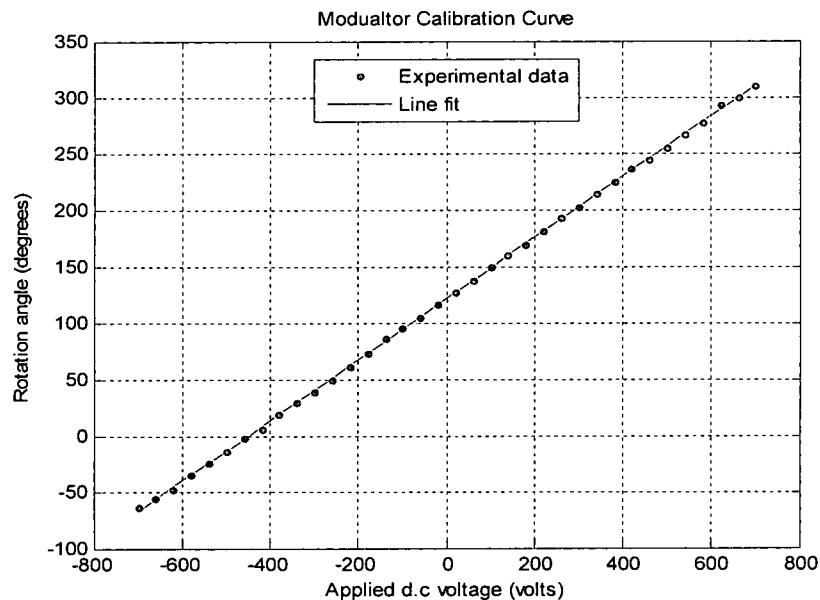


Figure 18. Polarization rotator calibration curve for a bias range of  $\pm 700$  volts. The bias voltage is in volts and the polarization rotation is in degrees. The rotation coefficient of the polarization rotator was found to be  $0.248^\circ/\text{volt}$ .

This value can vary significantly depending on how good the system alignment is. Therefore the alignment should be carefully (precisely) done if one is to expect an accurate calibration. Note that the line does not go through the (0,0) coordinate,

meaning that the crystal has some residual birefringence [14] due to the crystal itself.

Before looking at the evolution of the signal's amplitude change as the d.c bias changes, it is necessary to explain the steps involved in the generation of a circularly polarized light since the system operating principle uses this type of polarization. The steps in this task are associated with figure 19 shown below. Note that the alignment setup includes the beam splitter (BS) in order to pre-compensate for the polarization distortion it (the beam splitter) might introduce. The steps are:

1. The first polarizer (P1) and the second polarizer (P2) are inserted and one of them is rotated until a null is obtained. At this point P1 and P2 transmission axes are orthogonal.
2. The first quarter-wave plate (QWP1) is inserted and rotated until a null is seen on the screen. At this point the fast axis of this plate is parallel to the transmission axis of one of the polarizer. From the null position QWP1 is rotated by 45 degrees clockwise or counter-clockwise.
3. The second quarter-wave plate (QWP2) is inserted and rotated until a null is seen on the screen. At this point the light coming out of the beam splitter is quasi-circular due to a small ellipticity that the beam splitter introduces. QWP1 can then be adjusted to compensate for this ellipticity until the light that comes out of the beam splitter is almost perfectly circularly polarized. At that point there will be zero or almost zero intensity on the screen because P2 and QWP2 form a circular polarizer that cancels out the circular



polarization coming out of the beam splitter. After calibration P2 and QWP2 are removed.

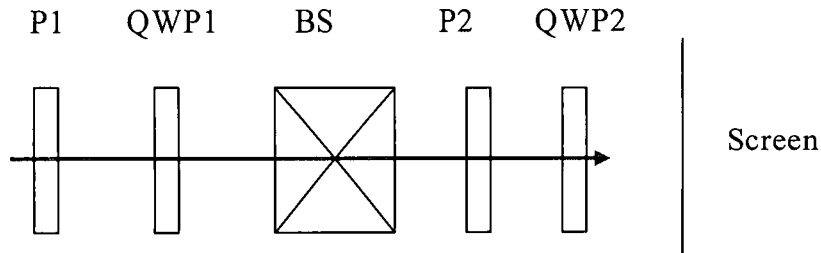


Figure 19. Setup used to generate circularly polarized light in the objective's back focal plane.

### C. Signal Testing and Processing

To have an idea on the behavior of the signal when different polarizations are used simulations of the first harmonic of the signal were performed. Figures 20(a), 20(b), 20(c), 20(d) show the results for various bias, orientation, and ellipticity angles. Equation (30) was used to simulate the signal behavior under different polarization and biasing conditions. In the simulations  $\Phi_b$  represents the rotation angle due to the d.c bias (see equation (29)) and, therefore, indirectly represents the d.c bias itself.  $\epsilon$  and  $\theta_0$  are the ellipticity and the orientation of the polarization ellipse, respectively. By adjusting these parameters different behaviors of the signal were observed in the time domain. The modulation depth in the signal was observed to be strongly dependent on the polarization. Of all polarizations tested the linear polarization produced the strongest modulation depth. In practice the incident beam has to pick up enough amplitude and phase on reflection in order for the signal to have a good modulation depth. These simulations are important in the

sense that they showed what to expect from the signal behavior before the real signal was tested.

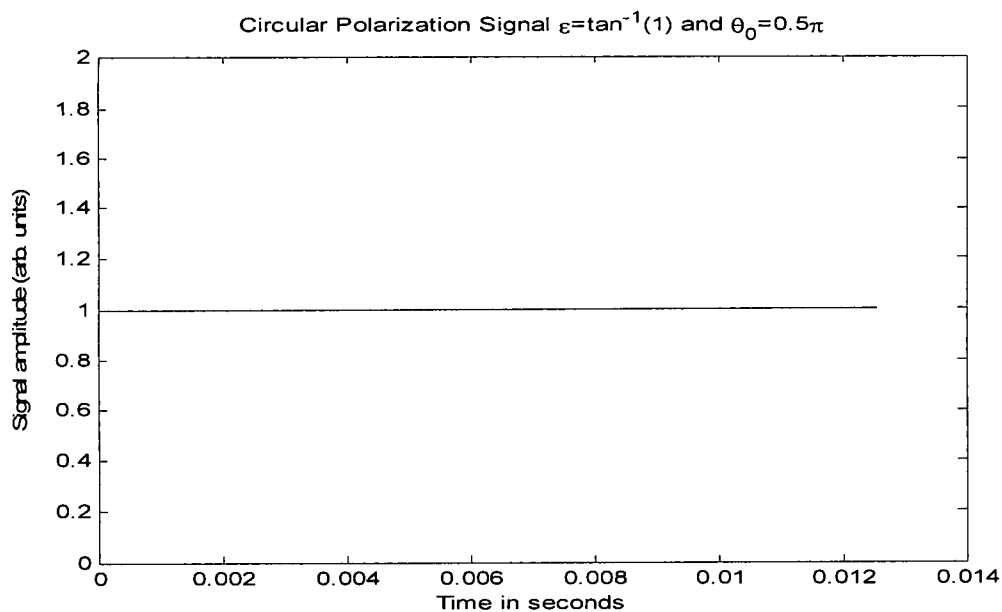


Figure 20(a). Detected signal amplitude when circular polarization is used.

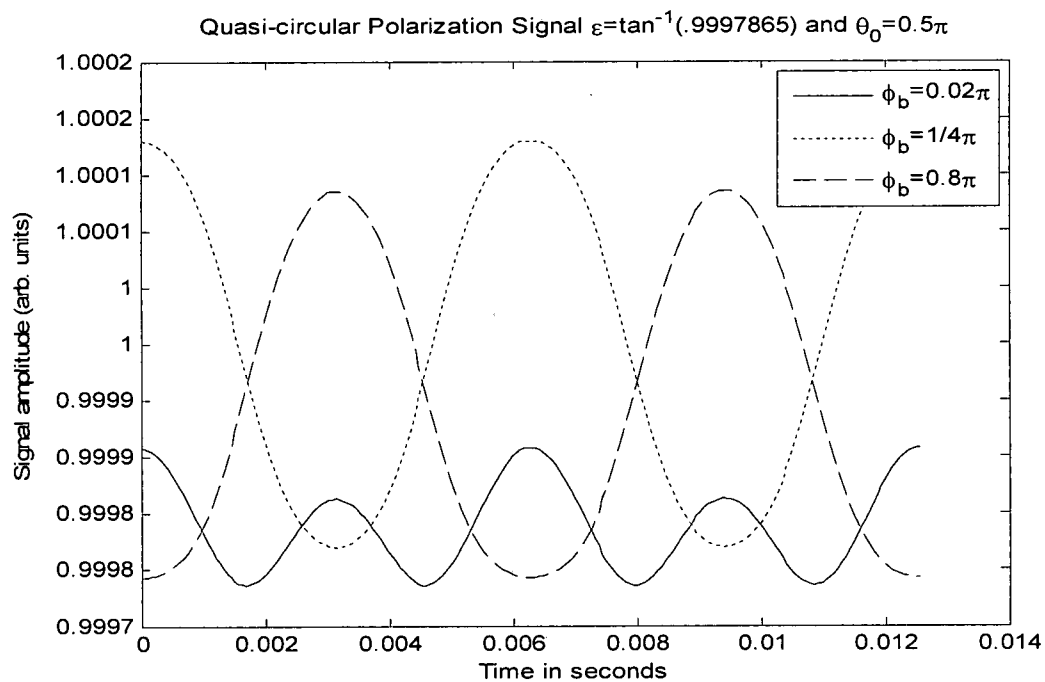


Figure 20(b). Detected signal when quasi-circular polarization is used.

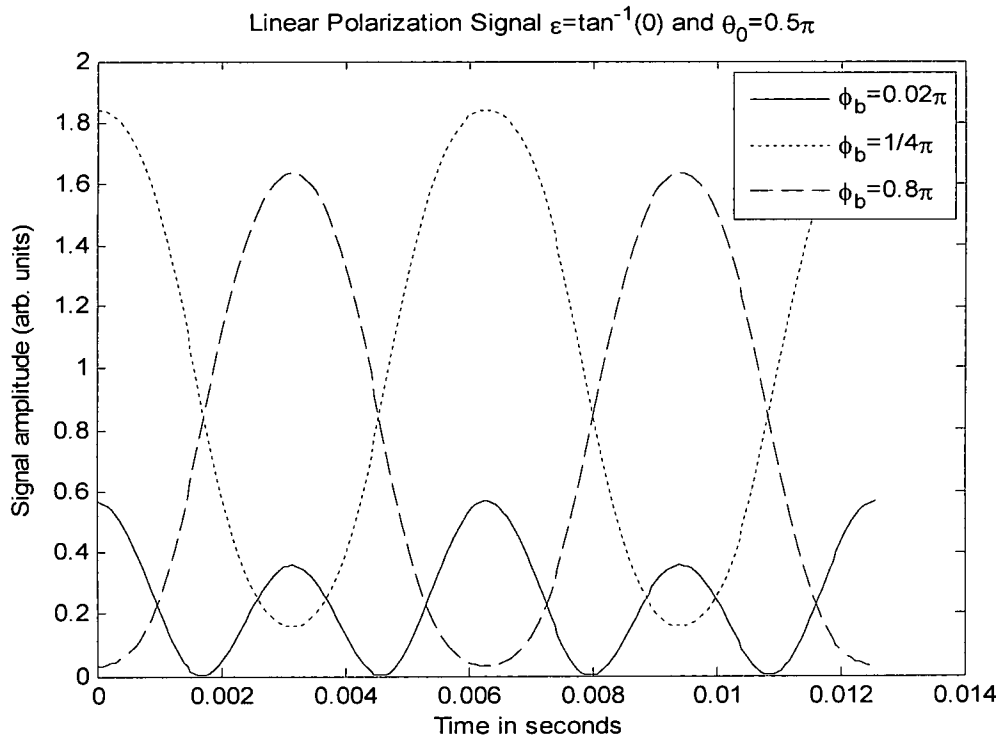


Figure 20(c). Detected signal when linear polarization is used.

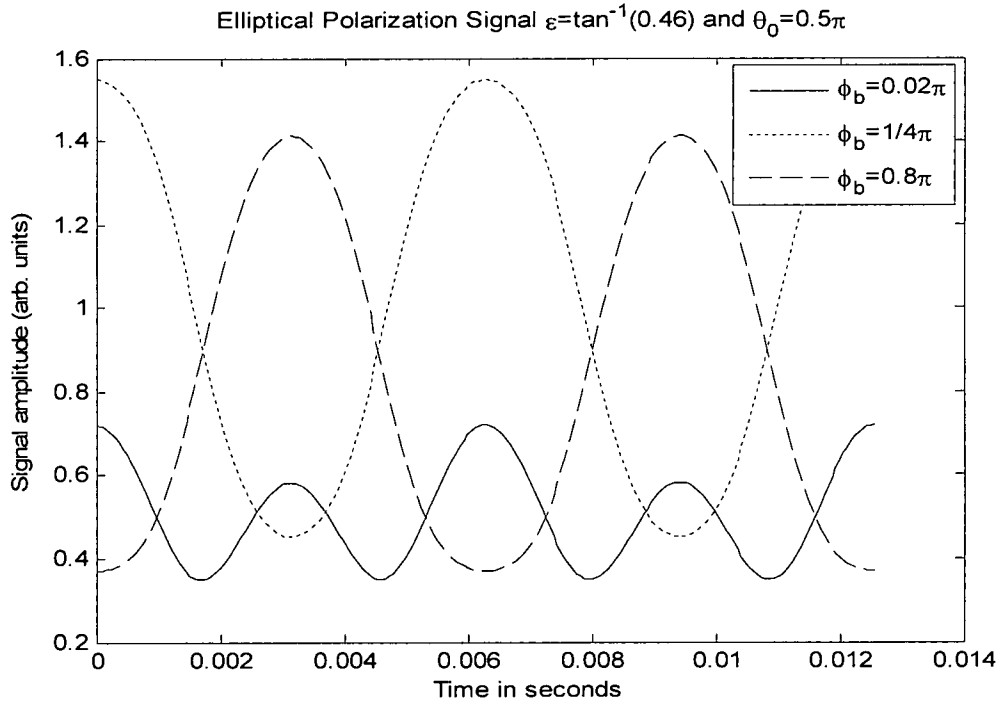


Figure 20(d). General polarization signal for different values of  $\Phi_b$ .

Figures 20(a), 20(b), 20(c), 20(d) show how the signal changes with time as the bias ( $\Phi_b$ ), orientation ( $\theta_0$ ), and ellipticity angle ( $\epsilon$ ) parameters are adjusted. Figure 20(a) shows no variation of the signal amplitude versus time. In this case a constant signal is expected due to the assumed circularly polarized light ( $\epsilon = 45^\circ$ ) coming from the sample. This means that if the sample does not introduce a phase in the beam on reflection the expected signal will flatten. For the case of quasi-circular polarization shown in figure 20(b) the signal will have a very poor modulation depth. The modulation is improved when linear and elliptical (general) polarizations are assumed as shown in figures 20(c), 20(d).

After the calibration and the alignment were done the microellipsometer signal was tested using a flat dielectric mirror in lieu of a sample. The signal was captured and displayed on the oscilloscope as shown in figure 21. The top signal shows the

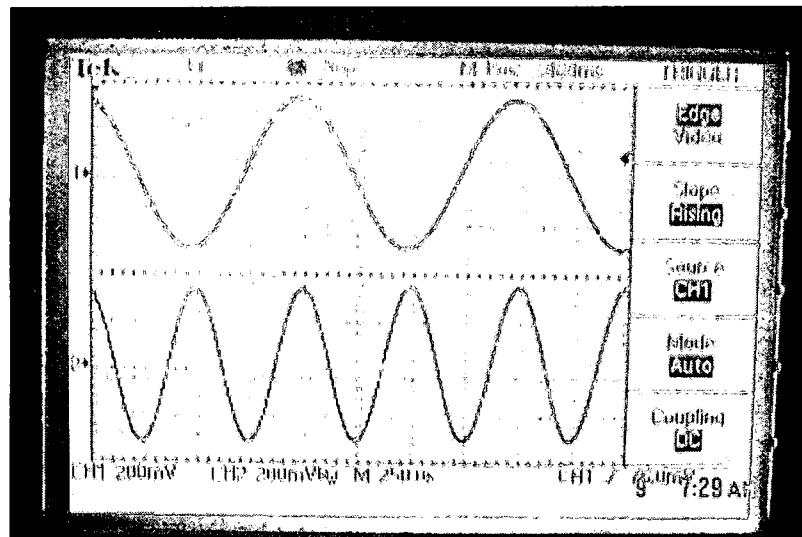


Figure 21. Modulation a.c voltage (top) and the detected 2<sup>nd</sup> harmonic signal (bottom) obtained while testing the polarization rotator and the null detection.

reference signal (a.c modulation voltage) and the bottom signal is the second harmonic component obtained by manually changing the d.c bias voltage across the

modulator. This result shows that the polarization rotator is performing properly. The illumination polarization used in this test was linear.

In principle the second harmonic has a very small amplitude (close to zero) when circular polarization is used for illumination. In figure 21 linearly polarized light was used for testing purpose and that is why the second harmonic has such a significant amplitude. In figures 22(a) and 22(b) the illumination polarization is circular and the sample consists of a silicon substrate coated with thin layer of photoresist on which some patterns have been etched. It can be seen that the signal passes from maximum amplitude to minimum amplitude (null or 2<sup>nd</sup> harmonic) as the d.c bias is adjusted across the modulator. The signals shown in these two figures were captured after a radial polarizer has been inserted in front of the detector. Note the low amplitude of the second harmonic in comparison to the one obtained in figure 21 using linearly polarized light, which is what we expected based on the

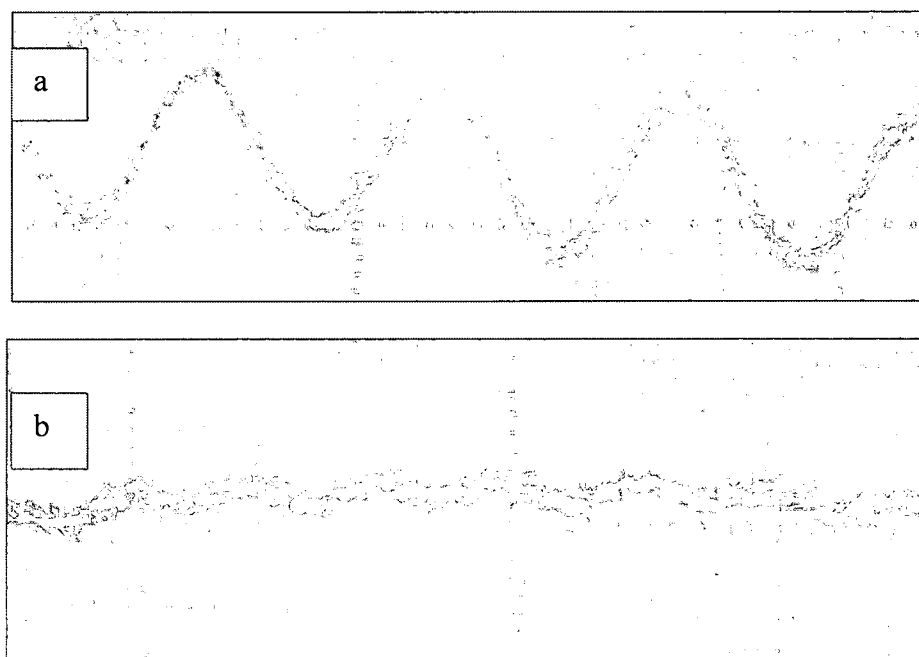


Figure 22: (a) Total signal; (b) Null occurrence (2<sup>nd</sup> harmonic)

signal simulations discussed earlier.

For processing purpose one period worth of signal is all that is needed to determine the minimum voltage at every scanned spot. Thus, the bias range was chosen so that the collected signal contains either two minima or two maxima. This arrangement leads to two possible signal shapes shown in figure 23(a) and 23(b) below. The processing algorithm was then developed in order to identify which shape the signal assumes, given a set of amplitude data. After the shape has been identified then the algorithm is set to track the minimum and record its value in file.

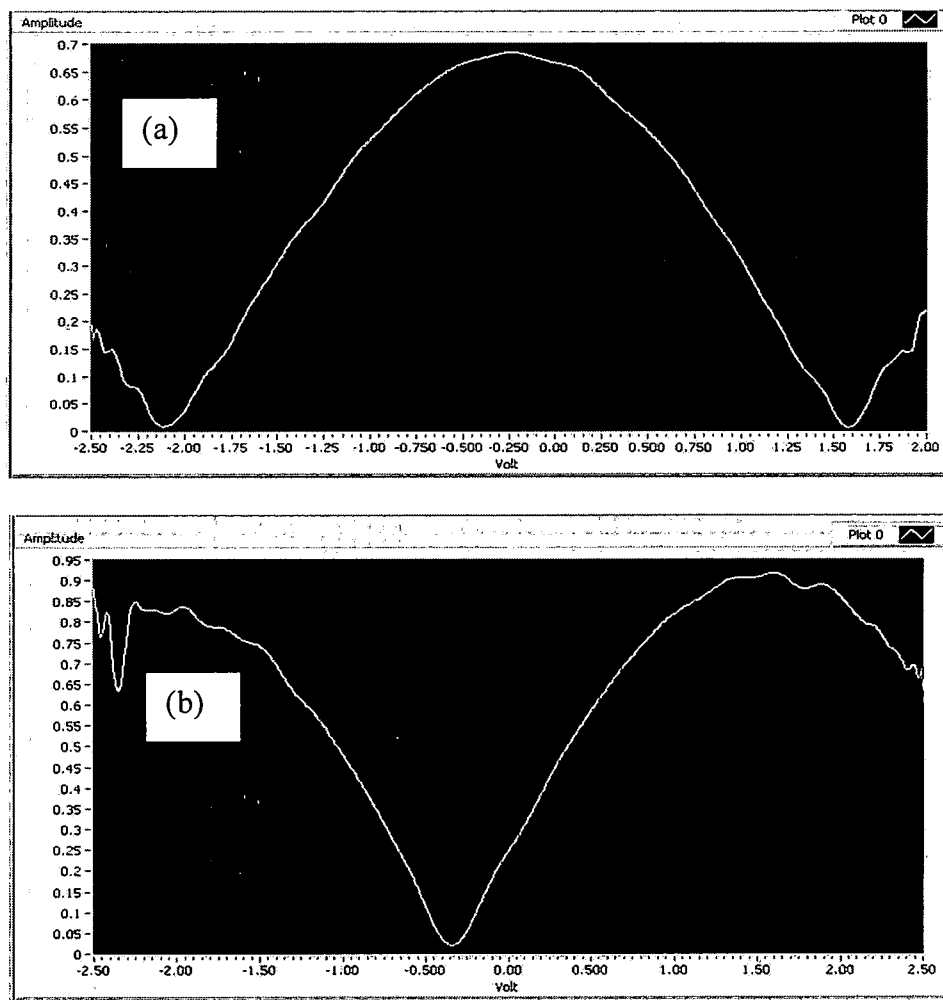


Figure 23: Signal shapes (a) Max-min-max case; (b) Min-max-min case.

In the case of the shape shown in figure 23(a) the requirement is to track only one minimum and record its voltage value as the sample is being scanned. It does not matter which minimum one chooses, be it the first or the second one. Ideally the two minima in figure 23(a) are 90 degrees apart (see signal derivation in chapter 3), but it was found that this may not be so under certain conditions explained later in this chapter. Identifying which shape the signal assumes might seem to be a straight forward task, but that is not true since the shape of the signal might drastically change and assume other shapes that the algorithm will not be able to identify. For small departures from the signal shapes shown in figures 23(a) and 23(b) the algorithm will perform as expected, but when the signal shape significantly departs from the two cases the algorithm will fail and false values of the minimum amplitude voltage will result. Therefore a robust algorithm is needed to deal with the task of identifying the shape of the signal. Since it's difficult to code each and every signal shape scenario into the algorithm, we tested the microellipsometer using a sample with a relatively smooth surface so that the signal shapes stay close to the "ideal" cases. When processing the signal if a shape is significantly different from the "ideal" shape the algorithm assigns a "red flag" value in the place of the minimum amplitude voltage to indicate a failure.

#### **D. Preliminary Results and Analysis**

In order to test the instrument we used a sample consisting of a silicon wafer covered by a thin layer of a photoresist on which some patterns were made using photolithography. Figure 24(a) shows a picture of a pattern on the sample that was

used to test the microellipsometer. The picture was obtained using a white light interferometer. The 3-D topology reveals that the lines forming the square patterns

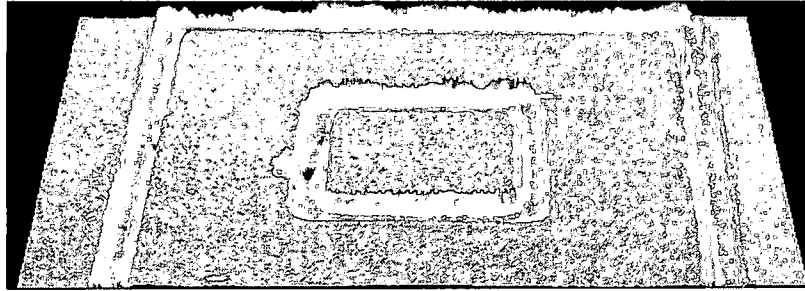


Figure 24(a). Pattern topography.

are trenches. Figure 24(b) is a line profile across the outer left side line pattern. The average trench width was measured to be about 2 microns and its average depth is about 120 nm.

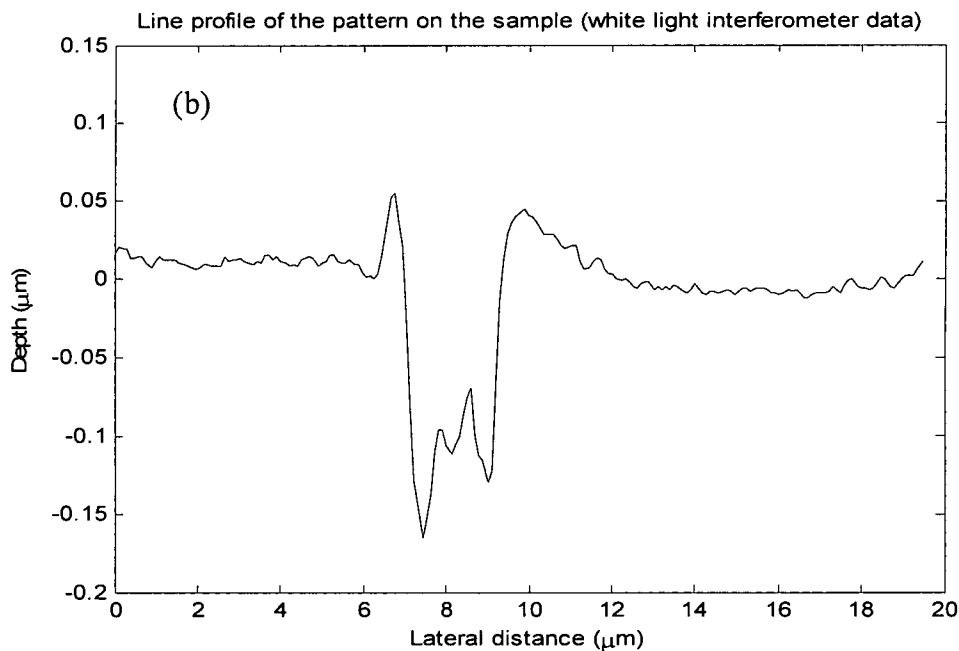


Figure 24(b) Line profile of a trench obtained using white light interferometer.

During the first test the microellipsometer was set to scan a distance of 25 microns. This distance was chosen so that a single line pattern can be traversed



from side to side. The step distance on the scanning stage was set at 0.8 micron, that is, the stage on which the sample is mounted was moving in steps of 0.8 micron while the sample is being scanned. The data was automatically collected and processed by the LabVIEW software. Figure 25 shows the result, i.e. the minimum amplitude

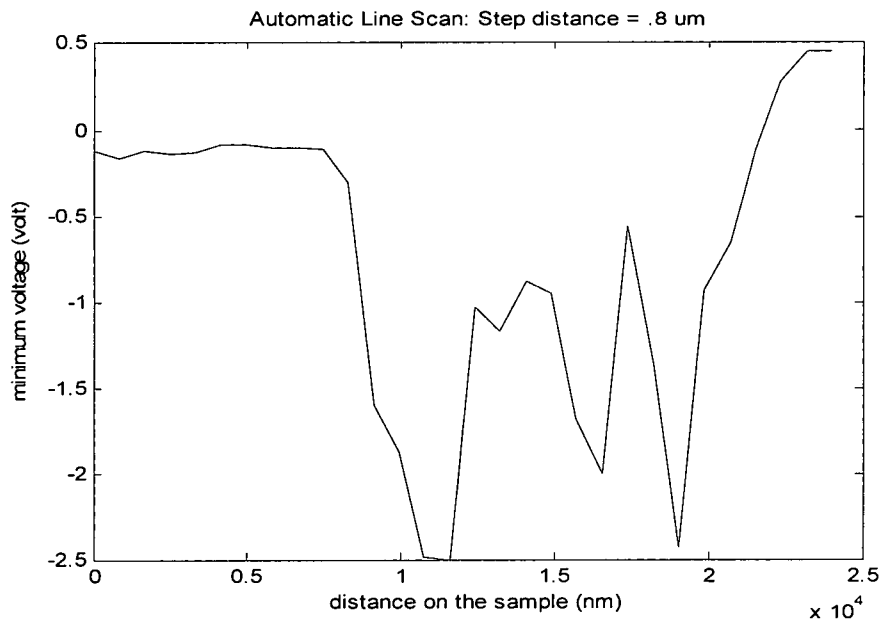


Figure 25. First test: minimum amplitude voltage vs. scanned.

voltage versus the scanned distance. Note that there is a region where the minimum amplitude voltage varies relatively smoothly; this is the edge region of the line pattern which is outside the trench region. Since there is no significant roughness there the signal shape stays almost constant and so does the minimum voltage. In the trench region the voltage starts oscillating due to the roughness in the region. The shapes of the signal in this region show significant departures from the “ideal cases” discussed earlier. The end of the trench region is not resolved in this result due to the roughness effect on the signal. The signal disruption and the sharp discontinuities arise when the beam encounters features that are smaller compared

to the beam's diffraction-limited spot size. Considering that the objective being used in the instrument has a numerical aperture of 0.95, and the illumination wavelength is 0.6328 micron, the lateral resolution we worked with is calculated and found to be 0.8126 micron. When the beam spot sits on a feature that is smaller than this resolution the polarization symmetry in the signal may be broken and, therefore, distorting the signal which, in turns, may cause the algorithm to fail. Using this resolution to sample the 2-micron wide trench region yields only 2 sampled data points. This means that any feature of size lesser than .8126 micron could not be resolved. The failure to resolve the right side edge of the trench is also due to the inadequate resolution and the roughness effect on the signal in the region. The gap region in figure 25 is about 10 microns wide which is about 5 times wider than the trench region width (2 microns) measured in figure 24(b). This confirms that the left side edge was not resolved. From this point on it became apparent that the system resolution and the roughness on the sample will significantly affect the result, although this was not totally unexpected.

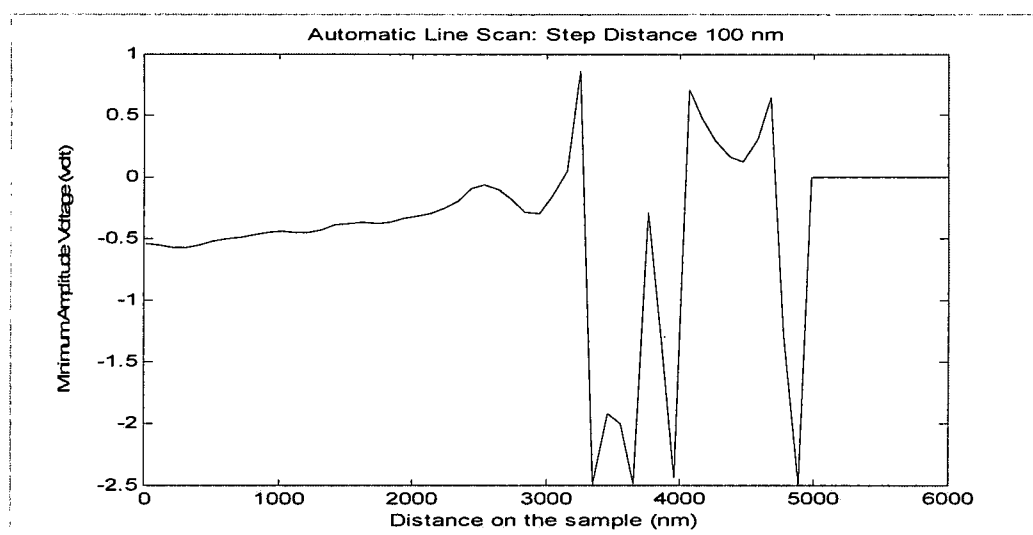


Figure 26(a). Repeatability test: min. amplitude. voltage vs. position.

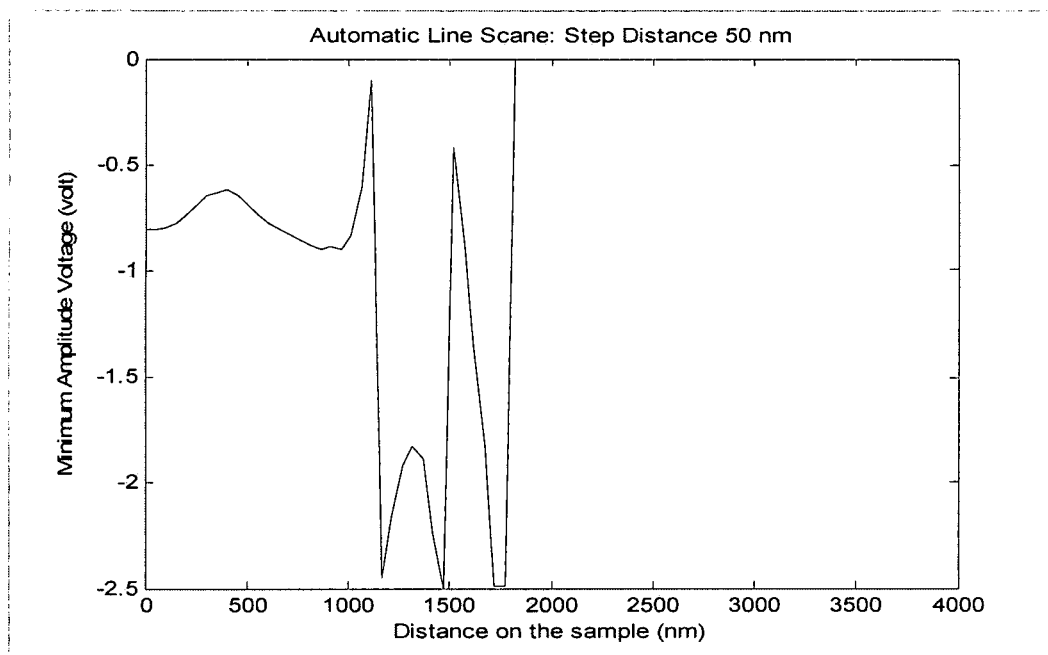


Figure 26(b). Repeatability test: min. amplitude voltage vs. position.

After the first test two scans were performed to test the repeatability of the result. On the first scan the system was set to scan a distance of 6 microns, including the trench width, using a step distance of 100 nm. The result of this scan is shown in figure 26(a). The second scan was set to cover 4 microns of the 6 microns scanned previously, using a step distance of 50 nm, in order to zoom in on the details seen in figure 26(a) and test the repeatability of the result. The result of the second scan can be seen in figure 26(b). The two scans were not run back to back since after the first scan the system was stopped in order to re-collimate the beam and adjust the scan parameters relative for the second scan. One can still see sharp discontinuities in the valley regions while the voltage varies smoothly in the flat regions. One major thing to notice in these results is that the last parts of the scanned distances have a completely flat minimum voltage (in these cases 0 volt). After investigation it was found that the processing algorithm systematically failed in those regions. The

visual inspection of the signal shapes revealed severe departure from the ideal shapes. But in the front edge regions the overall result shows an acceptable level of repeatability.

Apart from the resolution issue the second main issue is the algorithm failure. Figure 27(a) gives a ray picture of polarization symmetry disturbance when rays with different incidence angles reflect off a rough region. One can see that different rays are reflected in different directions with respect to their normal, thus causing diffuse reflections in addition to specular reflections. Since channels of our microellipsometer are treated in terms of rays this means the polarization symmetry would be disturbed when a surface is rough at the micron level. Even in the case where a feature size is on the order of the spot size, as shown in figure 27(b), the symmetry can be broken when the focal spot partially sits on a structure edge. The picture details are exaggerated to show that different reflection plans on the sample result in a defocused reflected beam. The signal's geometry shows that each one of the reflection angles corresponds to a different annular region in the lens pupil. This means that portions of the signal coming from each reflection angle is defocused and

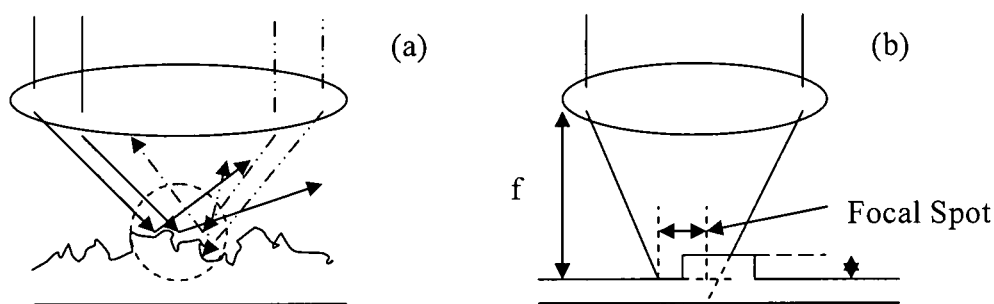


Figure 27. (a) Ray picture of reflection on a rough surface.  
(b) The focal spot seats on an edge.

has no symmetry. The defocused reflections are all collected by the lens and may

dominate the focused reflections, and the end result is a generally distorted signal. Under these conditions the shape of the total signal over a period will be far from the two ideal cases discussed earlier.

### **E. Manually Processed Data and Discussions**

For reason of time constraint on this work we chose to manually process the automatically collected amplitude data. The rest of the result shown from this point own was obtained through manual processing. By manual processing we mean going through the repetitive steps of determining the signal shape and determining minimum amplitude voltage.

Two more line scans were performed on two different areas of the sample. As said before, the data was manually processed, the results are shown in figures 28

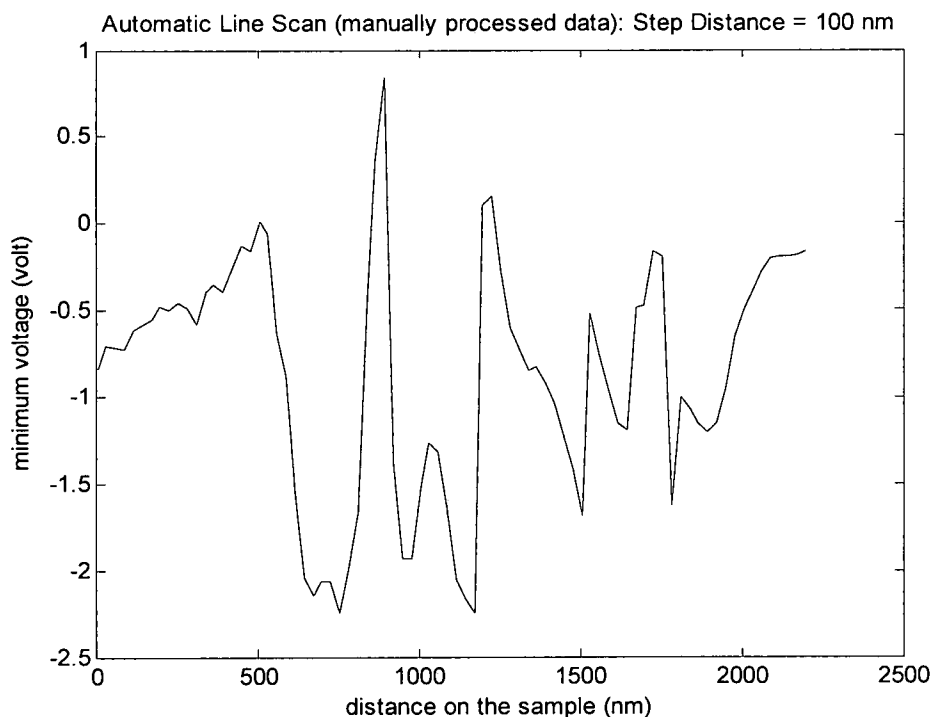


Figure 28. Manually processed data of the minimum voltage vs. scanned position on the sample.

and 30. The first scan in this category was conducted over a distance of 2.2 microns. This distance was enough cover only about .5 micron of the smooth region and the rest of the distance was enough to cover the width of the trench region. The step distance used in this scan is 100 nm and the result of this scan is shown in figure 28. As in the previous results here too one can distinguish the two regions, i.e. the left edge of the trench and the trench region. Sharp discontinuities are still present in the trench region while the edge region presents a relatively smooth variation of the voltage. Here too the left side edge was not resolved due to the difficulties that we explained earlier, but the overall behavior of the voltage is comparable to the one observed earlier in figure 25. The signal shape evolution with respect to the scanned distance was investigated by displaying the amplitude data as collected by the software. Displaying the amplitude data in this manner clearly revealed the general behavior of the signal in different regions and confirmed the claims we made based

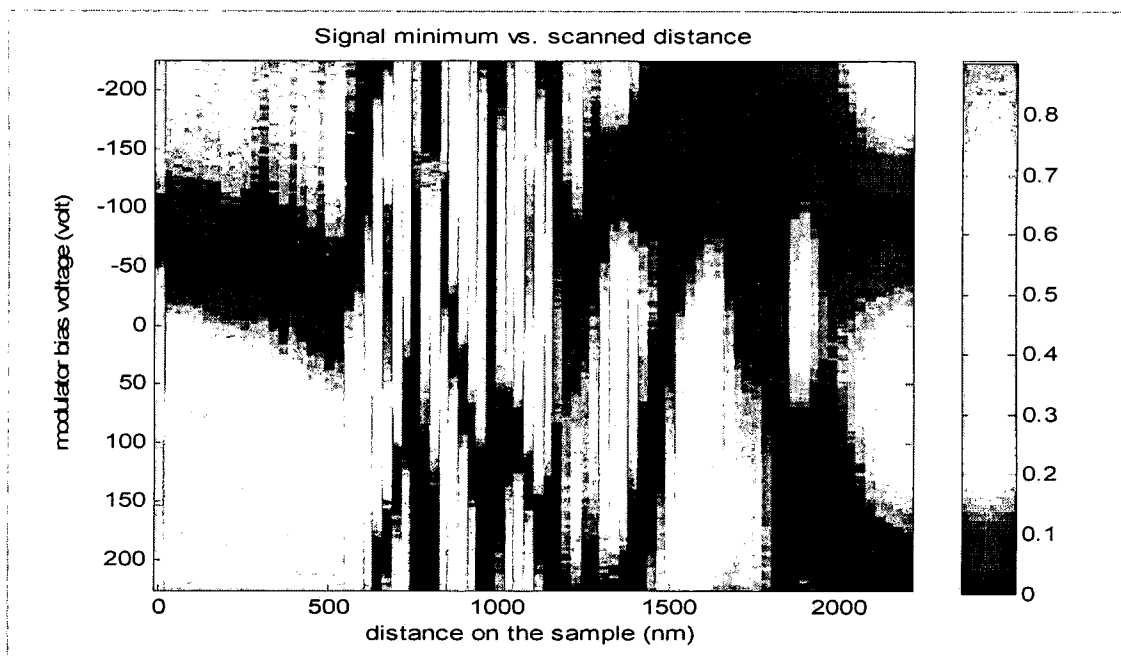


Figure 29. Signal amplitude data display. Dark regions are amplitude minima.

on the analysis of the minimum voltage data.

Figure 29 shown above shows the amplitude data used to produce the result displayed in figure 28. The dark blue regions show the spatial evolution (from left to right) of the minimum amplitude voltage. In the edge region of the pattern only one minimum is present (the signal assumes the shape in figure 23(b)), but passed the edge region one can clearly see that two minima are now present in the signal and their motions shows strong

oscillations in the trench region because of the roughness in the region. The inspection of amplitude data shows that there is significant loss of collimation in the beam shortly after the scanning had started. This is recognized by noting how the wide uniform bands of colors seen in the smooth region are abruptly discontinued starting at the location corresponding to the edge of the trench region. This discontinuity is very pronounced in the trench region. We investigated the origin of this collimation loss by collimating the beam and letting the system stay still for about 45 minutes (a typical scan might take longer or shorter than 45 minutes depending on the scan parameters) before checking the collimation. It was found that the reflected beam collimation significantly deteriorated. This is partially due to the fact that the objective may not have been firmly mounted that the sample plan was slipping out of focus as the sample was being scanned. Another very plausible cause would be that the sample was tilted with respect to the beam axis so that each position on the scan trajectory induced a defocus in the signal as the sample is being scanned. So, the loss of collimation is added to the list of issues already mentioned

earlier, however this problem can be easily fixed by using mounts that can firmly hold the sample and the objective.

To test the repeatability of the measurements the system was set to scan a distance of 10 microns on a flat region twice using a step distance of 200 nm. The two sets of

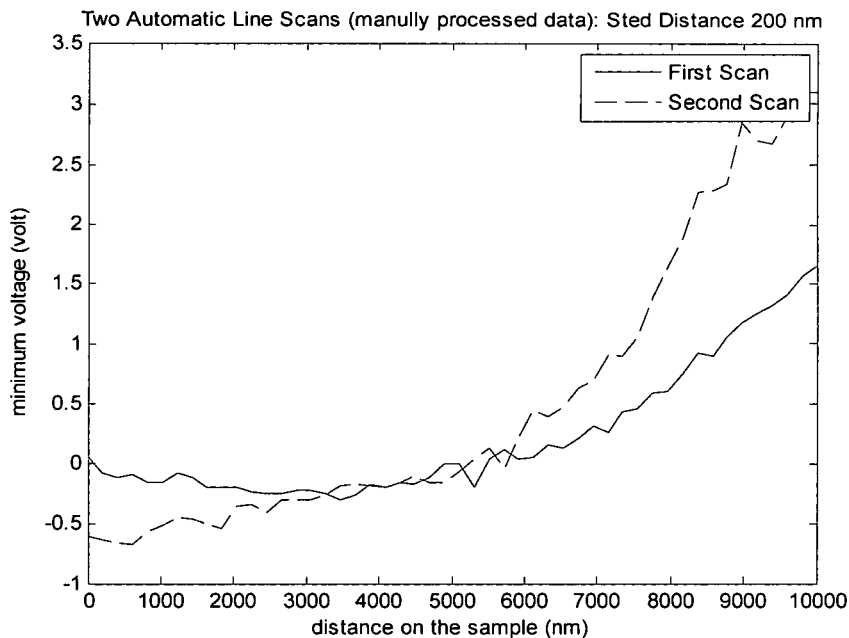


Figure 30. Repeatability test: minimum amplitude voltage vs. position on the sample.

data were manually processed and gave the results shown in figure 30. As noted in the previous results, the two scans yield similar but not exactly matching results. The trajectories are smoothly varying except for small local oscillations. These results are acceptably repeatable especially around the middle section of the trajectory. In both cases the voltage starts off relatively flat, but rises toward the end. This rise of the trajectories is believed to be caused by the combination of a loss of collimation and the tilted sample plane. In addition, the beam was calibrated slightly differently during each of the scan. However, in our design a small difference in collimation can still generate a significant difference in the results. In



this case roughness is excluded as one of the causes since the scanned region was relatively smooth, however the voltage general behavior is comparable throughout for both scans.

Lastly, we sought to investigate the consistency of the collimation loss by performing two scans on the same location on the sample, and then displaying their amplitude data as was previously done in figure 29. The results are shown in figures 31(a) and 31(b) below. The signal data in both figures shows two minima (dark regions) at the beginning, but additional minima appear in the trench region. It is also necessary to note that the almost constant spacing between the two minima trajectories observed at the beginning quickly disappear in the trench region due to the oscillation. Figures 31(a) and 31(b) show these trajectories pulling toward each other and away from each other in the rough regions. A qualitative and quantitative in-depth study of the dynamics of this behavior is important in order to characterize the signal behavior when one is working with a rough sample. In both figures a third minimum starts arising around the trench region. We have no definite answer as to why this minimum has shown up, but one might inconclusively say it is caused by the roughness-induced defocus and the broken polarization symmetry. The bright continuous bands at the left side in both figure 31(a) and figure 31(b) indicate the region where the beam collimation is good. The figures indicate that the collimation is lost when the beam start scanning the trench region. So, the loss of beam collimation contributed in a major way to the failure to resolve the trench and the right side regions.

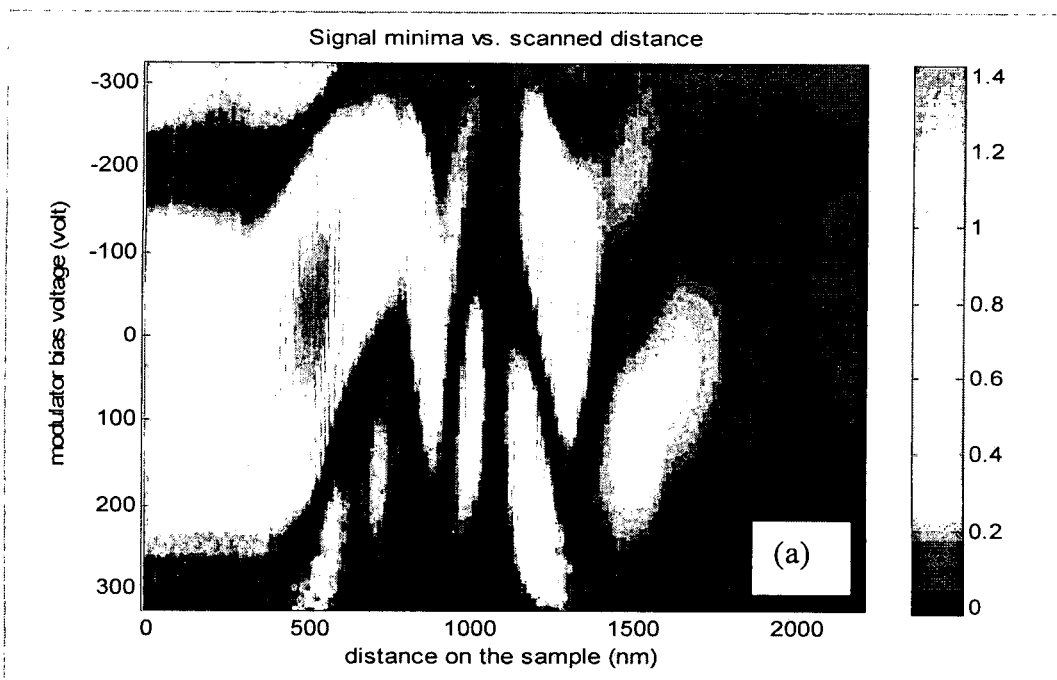


Figure 31. (a): Signal amplitude data: Amplitude evolution in bias voltage and location on the sample. The dark regions show the evolution of the minima.

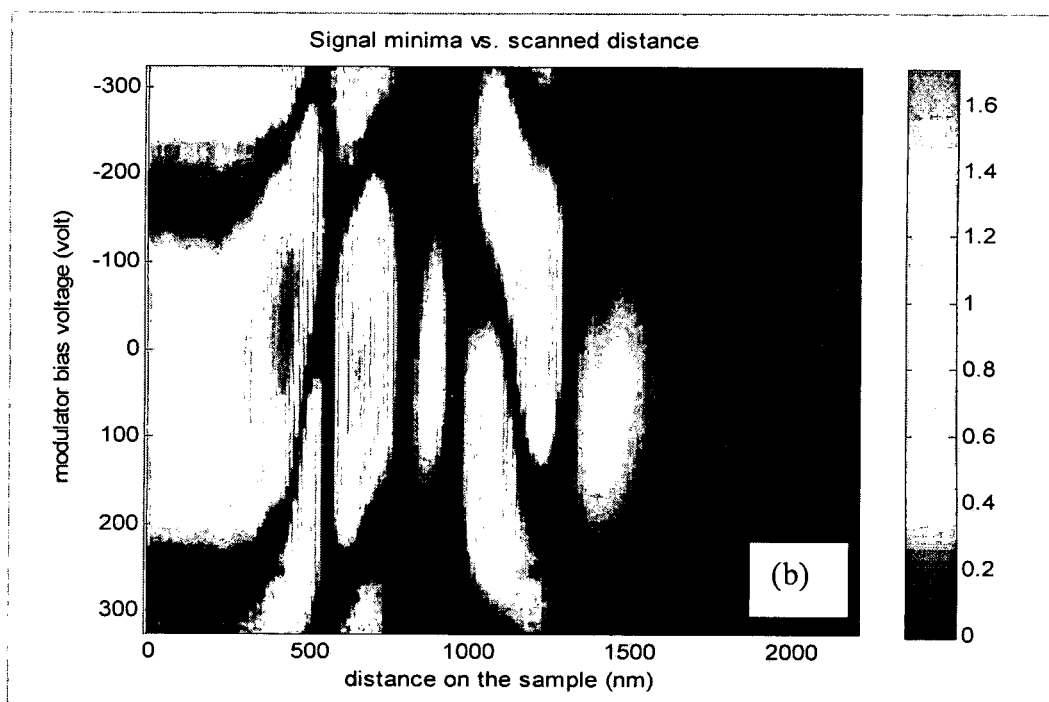


Figure 31.(b): Signal amplitude data: Amplitude evolution in bias voltage and location on the sample. The dark regions show the evolution of the minima.

## **F. Summary**

The objective of this research was to build and test a nulling microellipsometer using a polarization radial symmetry. We have demonstrated that a microellipsometer can be built based on the rotational polarization symmetry concept using a variable circular retarder. Various scans were performed and the results were discussed. Although the results presented above are not optimal, they corroborate the fundamental functional principles upon which the instrument is based. The nulling scheme has worked as expected by producing amplitude minima in the signal. Though the circular symmetry scheme has resulted in an acceptable signal level, the behavior of the signal (polarization) when scanning rough surfaces, is an important issue that needs to be qualitatively and quantitatively investigated. Understanding this issue will lead to corrections that will optimize the instrument performance. The results presented above show that the instrument can take more accurate measurements once the issues mentioned earlier are corrected and the instrument performance is optimized.

## **CHAPTER V**

### **FUTURE WORK**

#### **A. Signal Strength and Quality**

There is still considerable work to be done in order to improve the level and the quality of the signal being detected. It is true that these two parameters do vary depending on the characteristics of the sample under investigation, but an overall good signal level is always very important to start with. The beam cleaning and collimation optics can be modified to decrease the collimated beam diameter so that the beam intensity is higher. This will help compensate for the intensity loss at multiple surfaces that the beam (especially the reflected beam) crosses on its way from the sample to the detector. This improvement combined with an optimal alignment of the system will increase the signal level at the detector. An optimal alignment of the optical elements is very important for this system because of the role that polarization symmetry plays. A poor alignment would disrupt the symmetry and kill the useful signal. The results presented in chapter four were obtained without using an annular aperture due to the low level of the signal at the detector. In the future, after optimizing the signal, we will insert an annular aperture between the radial analyzer and the detector as planned in the design. More importantly we will need to stabilize the objective and sample by using a

better mounts for the objective and the sample. When the objective and the sample are well mounted the defocusing and the collimation loss issues will be solved.

As mentioned several times in chapter four, it is imperative to study the behavior of the signal on rough surfaces. This may be done by studying the reflection (scattering) of a polarized, normally incident focused beam on a rough surface. The goal will be to study how the polarization and the amplitude of the incident beam are affected under those circumstances. Incident fields on a rough sample can be modeled using well established equations of fields propagation [15]. The resulting output can be used as an input to a model developed using a software package like COMSOL Multiphysics[16], and the reflected fields can then be used to synthesize the information carrying signal. This simulation, if successfully carried out, will provide a much better insight on the origin of the seemingly strange signal behavior mentioned in chapter four. In addition, the roughness-induced signal symmetry disturbances may be exploited to super-resolve subwavelength features.

#### **B. Using Radially Polarized Light for Sample Illumination**

Using a simple dielectric mirror as sample, it was found that for circular or quasi-circular polarizations the detected signal has a poor modulation depth; that is, the signal is almost completely flat. But, when the incident polarization is linear, the modulation depth improves significantly. Unless the sample introduces a significant polarization change in the signal upon reflection, circular polarization illumination will be hard to work with when examining very thin samples. Since one does not know in advance the thickness of the sample, circular polarization illumination will

produce unreliable measurements if a sample turns out to be very thin. Figures 32(a) – (d) show examples of the effect of circular and quasi-circular polarizations illumination. One can see that the signal modulation is very poor at at start. From (a) to (d), when a gradually growing ellipticity is introduced in the signal by adjusting either the first QWP or the first polarizer (see figure 15) by an incremental amount of  $1^\circ$ , the modulation starts to improve. By exploiting the built-in polarization symmetry of a radially polarized beam, the signal modulation can be improved and thin samples can be characterized more accurately. Figure 33 shows

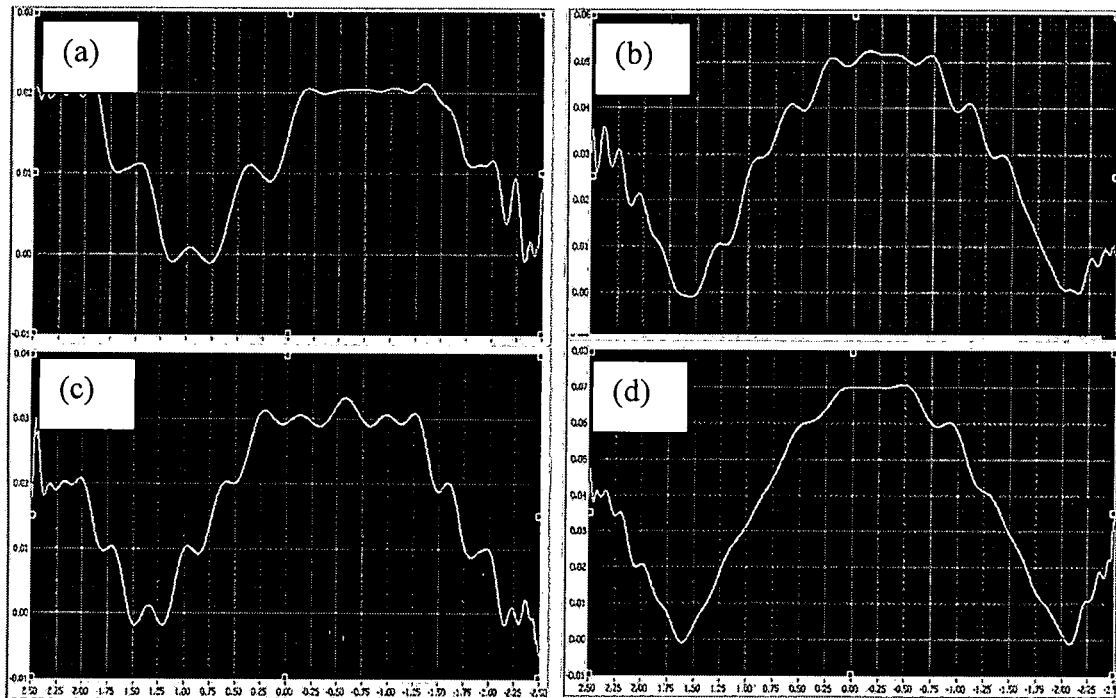


Figure 32 (a) – (d). Signals produced by circular and quasicircular polarizations.

a set up for radial polarization illumination. Starting with a cylindrical vector beam (CV beam) a radially polarized beam can be generated using two half-wave plates (HWP) [4] as show in the figure's lower inset. This radial polarization goes through the objective to the sample. In each channel's coordinate system the polarization

essentially be linear. On reflection the linear polarization in each channel picks up a phase and becomes generally elliptically polarized while the total signal still has a good modulation depth due to a strong ellipticity ( $\epsilon = 45^\circ$ ) in each channel. Several methods of generating radially polarized beams have been reported [17, 18]. Some are simple but most are too complex to be implemented for use on a microellipsometer system. We are interested in finding ways of generating this sort of beam in an efficient way as far as cost and implementability are concerned.

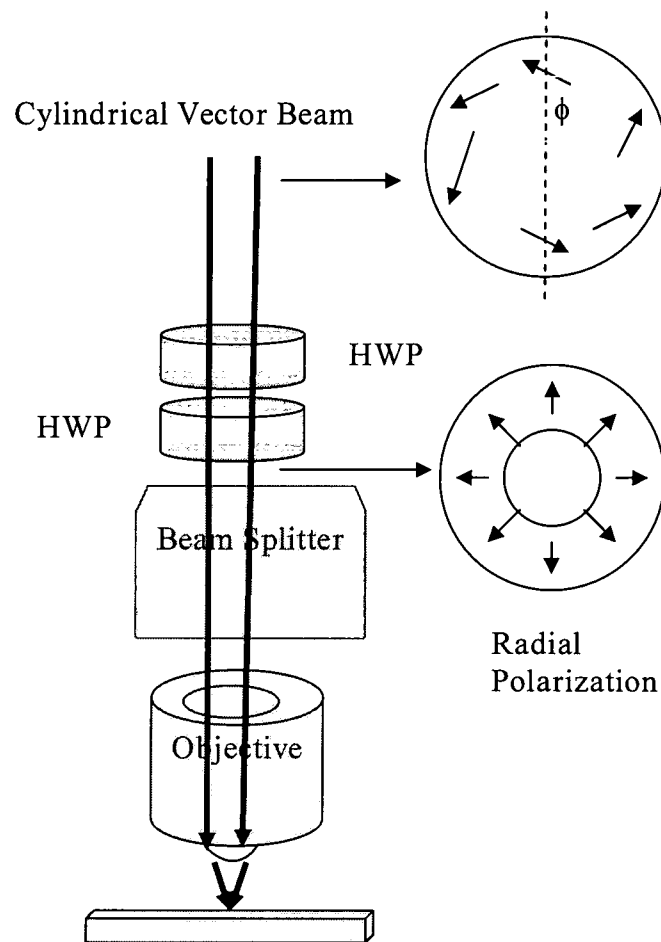


Figure 33. Radial polarization illumination.  
HWP: Half-wave plate.

### **C. Calculating the Optical Properties**

The final goal in ellipsometry is to measure a sample's optical properties such as the refractive index and the thickness. In this work the effort was limited to practically demonstrating the principles of a nulling microellipsometer using a polarization symmetry concept. Eventually the goal is to go beyond a simple demonstration, develop a regression algorithm that takes in the surface-mapped minimum voltage data and calculates the refractive index and the thickness of the sample under examination.

### **D. Improving the User Interface**

Last but not least is the goal to build a user friendly interface of the instrument. The current user interface is not as easy to use since it's been developed by modifying a pre-existing interface. This is also true for most of the instrument drivers. The decision to use pre-existing codes was motivated by the need to speed up the implementation of the instrument, but if time allows a custom built software and user interface will eventually be developed to specifically address the functionality of our instrument.



## BIBLIOGRAPHY

1. R.M.A. Azzam and N.M. Bashara, *Ellipsometry and Polarized Light*. North Holland, Amsterdam. Chapter 3 (1977).
2. Wolf and Born, *Principles of Optics: Electromagnetic Theory of Propagation, Interference, and Diffraction of Light*. 6<sup>th</sup> edition. Pergamon . Chapter 1 (1980)
3. Harland G. Tompkins, *A User's Guide to ELLIPSOMETRY*. Academic Press. Chapter 1 (1993).
4. Q. Zhan and J. R. Leger, "Microellipsometer with radial symmetry," *Appl. Opt.* **41**, pp. 4630 – 4637, (2000).
5. Gerald E. Jellison, Jr. and Frank A. Modine. *Handbook of Ellipsometry*. Ed. Thomas Harland and Eugene A. Irene. Springer. pp. 470 (2005).
6. Stoyan C. Russev and Tzanimir VI Arguirov, "Rotating analyzer – fixed analyzer ellipsometer based on null type ellipsometer", *Rev. Sci. Instrum.* **70**, pp. 3077 - 3082 (1999).
7. J. Monin and G. A. Bountry, "Conception, Realisation, et Fonctionnement d'un Nouvel Ellipsometre." *Nouv. Rev. Optique* **4**, pp. 159 – 169 (1973).
8. M. Erman and J. B. Theeten, "Spatially Resolved Ellipsometry", *J. Appl. Phys.* **60**, pp 859 – 873 (1986).
9. An-Hong Liu, P. C. Wayner, and J. L. Plawsky, "Image Scanning Ellipsometry for Measuring Nonuniform film thickness profiles", *Appl. Opt.* **33**, pp. 1223 – 1229 (1994).
10. Chung Wah See, Michael G. Somekh, and Richard D. Holmes, "Scanning Optical Microellipsometer for pure surface profiling", *Appl. Opt.* **35**, pp. 6663 – 6668 (1996).
11. J. M. Leng, J. Chen, J. Fanton, M. Senko, K. Ritz, and J. Opsal, "Characterization of Titanium Nitride (TiN) films on Various Substrates Using Spectrophotometry, Beam Profile Reflectometry, Beam Profile Ellipsometry and Spectroscopic Beam Profile Ellipsometry.", *Thin Solid Films* **313** , pp. 303 – 313 (1998).

12. International Technology Roadmap for Semiconductor, 2003 Edition,  
<http://public.itrs.net>.
13. Q. Zhan and J. R. Leger, "Interferometric Measurement of Berry's Phase in Space-variant Polarization manipulations," *Opt. Comm.* **213**, pp. 241-245, (2002).
14. Yew Li Hor and Qiwen Zhan, "Calibration of an electro-optics variable circular retarder with application in nulling microellipsometer", *SPIE proceedings*, Vol. **4**, pp. 5392-28 (2004).
15. J. R. Leger and Q. Zhan, "Focus shaping using cylindrical vector beams", *Opt. Exp.* **10**, pp. 324-331 (2002).
16. <http://www.comsol.com>
17. A. V. Nesterov, V. G. Niziev, and V. P. Yakunin, "Generation of high-power radially polarized beam", *J. Phys. D: Appl. Phys.* **32**, 2871-2875 (1999).
18. T. Wilson, F. Massoumian, and R. Juskaitis, "Generation and focusing of radially polarized electric fields", *Opt. Eng.* **42**, pp. 3088-3089 (2003).

R002592254